Smart Materials and Structures

PURPOSE-LED PUBLISHING™

PAPER • **OPEN ACCESS**

Compo-code 3D/4D printing of shape-memory meta-composites for supreme precision, speed, recovery, and energy dissipation

To cite this article: O Kordi *et al* 2025 *Smart Mater. Struct.* **34** 085007

OPEN ACCESS
IOP Publishing
Smart Materials and Structures
Smart Mater. Struct. **34** (2025) 085007 (22pp)
https://doi.org/10.1088/1361-665X/adf37d

Compo-code 3D/4D printing of shape-memory meta-composites for supreme precision, speed, recovery, and energy dissipation

O Kordi[1], M Yusefi Passandi[1,2], A H Behravesh[2] and M Bodaghi[1,*]

[1] Department of Engineering, School of Science and Technology, Nottingham Trent University, Nottingham, United Kingdom
[2] Faculty of Engineering and Applied Science, Ontario Tech University, Oshawa, Canada

E-mail: mahdi.bodaghi@ntu.ac.uk

Received 20 May 2025, revised 2 July 2025
Accepted for publication 23 July 2025
Published 6 August 2025

Abstract

This study introduces a groundbreaking methodology for 3D/4D printing of continuous fiber-reinforced meta-composites, achieving unprecedented precision and performance through the development of custom G-code modifier software. This novel software, which automatically detects part edges and locally reduces printing speed, creates a modified G-code so-called compo-code for printing composites. This represents a breakthrough in composite additive manufacturing by significantly enhancing fiber alignment, printing quality, and reducing print time. These innovations enable the fabrication of high-performance lattice composites with optimized energy absorption, dissipation, and shape recovery capabilities. This research examines hexagonal and re-entrant meta-composites reinforced with continuous glass fibers (0, 20, 40 wt%) to evaluate their thermo-mechanical behaviors. Results demonstrate that meta-composites printed with the compo-code achieve approximately remarkable tensile (2700 N), bending (200 N), and compressive (400 N) forces compared to conventional methods. Comparing meta-composites with non-reinforced meta-structures, the tensile, bending, and compression strengths rise by 1000%, 1000%, and 450%, respectively. Hexagonal patterns exhibit superior tensile and bending strength, while re-entrant patterns, with their auxetic behavior, achieve supreme compressive performance and demonstrate a stable quasi-constant force plateau, critical for efficient energy absorption and dissipation. Hexagonal meta-composites with 40 wt% fibers deliver the highest energy dissipation and absorption (0.51 J and 0.10 J). Additionally, shape recovery tests under compression and bending reveal recovery ratios of 100% for non-reinforced and ∼95% for reinforced samples. By integrating advanced software, meta-material design, and continuous fiber reinforcement, this study provides a transformative framework for high-precision manufacturing of next-generation meta-composites, paving the way for advanced applications.

* Author to whom any correspondence should be addressed.

Keywords: glass fiber-reinforced composites, shape memory meta-composites, 3D/4D printing, energy absorption, tool path design

1. Introduction

The Greek prefix 'meta' means 'beyond'; hence, meta-material implies a man-made structure designed to show unique properties that cannot be found in nature [1–3]. Metamaterials are engineered materials which their unique properties such as effective thermal properties [4, 5], negative Poisson's ratio [6], variable softening/ hardening [7] and unusual dynamic behaviors [8, 9] arise from their internal architecture rather than their composition. While many metamaterials are based on periodic unit cells, a broader definition includes graded [10], hierarchical [11], and non-periodic or stochastic architectures [12], which can also achieve unconventional mechanical, thermal, or acoustic responses. The unique properties of metamaterials support a wide range of applications such as energy absorption, impact resistance, vibration damping, and bio-scaffolding [13–15].

Energy absorbing structures play a significant role today and many natural energy absorbing structures such as bones, woods, teeth, and hooves can be found in the nature [16]. Energy absorbing meta-materials are widely used across various industries such as aerospace [17], automotive industry [18], civil engineering [19], sport protection equipment [20], medical devices [14], and energy sector [21]. Figure 1 shows different applications of meta-material composites or so-called meta-composites in various industries.

Meta-materials are capable of absorbing a significant amount of energy without producing elevated stress levels by experiencing significant compressive strains at nearly constant stress levels [22]. The ability to transform kinetic energy into different forms of energy through elastic and/or plastic deformations, mechanical instability, and structural collapse is provided by the energy absorption principle in meta-materials and lattice-based structures. The most efficient traditional technique for absorbing energy among the different energy absorption methods has been plastic deformation in ductile materials like metals and polymers [23, 24].

The majority of meta-material applications have not yet been fully utilized due to the current lack of manufacturing processes capable of producing large-scale meta-materials with complex geometries [25]. Nevertheless, advancements in additive manufacturing (AM) are anticipated to result in much wider adoption of metamaterials in daily life in the future [1]. One of the most popular AM techniques for the fabrication of meta-materials is fused deposition modeling (FDM). By depositing the extruded molten thermoplastic polymer on the print surface in accordance with the specified paths from the computer-aided design (CAD) model, the FDM process creates complex parts layer-by-layer [26, 27]. Because FDM printed objects are made layer-by-layer, their mechanical properties are lower than those made using traditional techniques like plastic injection and machining [28]. Although research on using many techniques to enhance the mechanical properties of printed parts has been conducted recently, printing parameter optimization, nanoparticle addition, and continuous fibers have all been presented as effective approaches [29–32].

One of the main approaches for using continuous fibers in FDM process is the simultaneous impregnation technique, or *in-situ* impregnation. It was a promising approach to enhance the mechanical properties of parts which are printed by FDM [33]. Akhoundi *et al* [34] investigated the impact of volume fraction of glass fiber on mechanical properties of parts that are printed by simultaneous impregnation technique. The results show that by using 30% glass fibers, the analyzed PLA's tensile strength and elastic modulus increased by five times (from 59 to 296 MPa) and six times (from 3.5 to 20.8 GPa), respectively [34, 35]. On the other hand, most of the printed parts with simultaneous impregnation technique have a simple geometry and it is challenging to print complex parts with high precision and sharp edges and the surface quality of samples was often undesirable [36–38].

While various approaches have improved mechanical performance, achieving adaptive or responsive behavior in printed composites has remained limited. Therefore, recent studies have increasingly focused on integrating shape memory polymers (SMPs) and adaptive functionalities into printed composites, a concept known as 4D printing [14, 39]. As traditional 3D printing technologies have grown, 4D printing has been entering into the AM era [40]. The fourth dimension corresponds to 'shape change' that occurs as 3D printed parts change over time. Xin *et al* [39] provided an extensive review of the mechanical models of SMPs, SMP composites, and SMP nanocomposites, as well as their uses in 4D printing and space deployable structures. Several studies have been carried out to offer reconfigurable mechanical single material meta-structures with impact-mitigation capabilities using 4D printing technology [41, 42].

Despite significant advancements in 3D/4D printing, achieving high-precision manufacturing of continuous fiber-reinforced meta-materials remains a formidable challenge, especially for applications demanding exceptional energy absorption, recovery, and structural integrity. Addressing this challenge requires not only advancements in manufacturing processes but also the careful selection of reinforcement materials that balance strength, affordability, and suitability for AM techniques. Among available options, glass fibres glass fibers have been widely reported as a practical reinforcement due to their favorable combination of high strength-to-weight ratio, cost-effectiveness, and compatibility with extrusion-based 3D/4D printing processes [34, 35]. While carbon fibers offer superior strength and stiffness, their higher cost and brittleness can limit processability and make them less suitable for applications where impact resistance and ductility are important [32]. Aramid fibers, such as Kevlar,

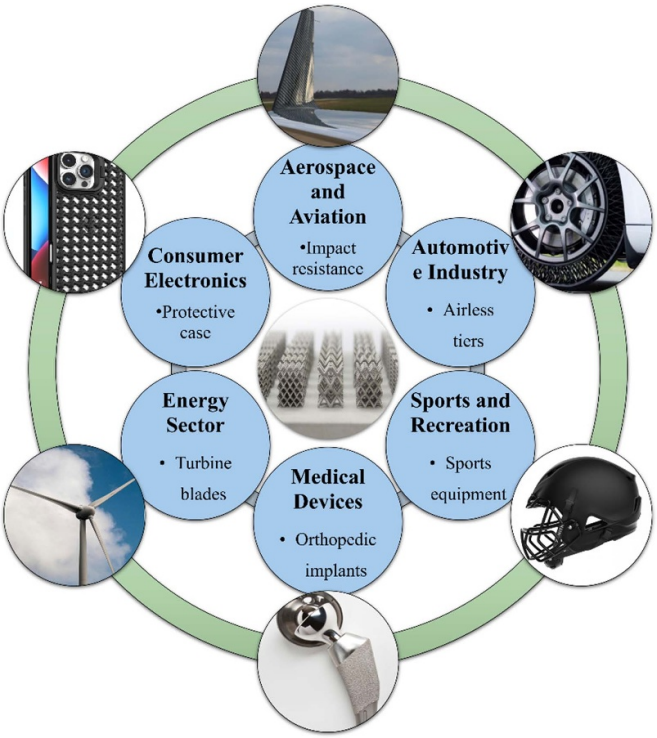

Figure 1. Application of meta-composites.

provide excellent toughness and energy absorption, but present challenges in handling and impregnation due to their flexibility and surface chemistry [43].

Although various methods have improved mechanical properties and demonstrated shape memory effects in printed composites, achieving high-precision manufacturing of fiber-reinforced meta-materials with complex geometries and tunable reinforcement levels remains challenging. To bridge this gap, this study contributes to composite science and engineering by developing a novel G-code modifier software package to generate a new tailored G-code so-called compo-code for simultaneous impregnation 3D/4D printing. The software automatically detects part edges and dynamically adjusts the printing speed, enhancing precision, fiber alignment, and printing quality while maintaining efficiency. Additionally, this research investigates the mechanical properties, energy absorption/dissipation, constant force feature and shape recovery of hexagonal and re-entrant patterned meta-composites with varying glass fiber volume fractions (0, 20, and 40 wt%). The findings of this study provide new insights into the design and manufacturing of high-performance meta-composites, enabling broader applications in energy absorption systems, biomedical devices, and automotive/aerospace engineering.

2. Materials and methods

2.1. Equipment and procedure

Prusa MK4S 3D printer was used, and its extruder was modified for printing the continuous fiber-reinforced composites based on simultaneous impregnation technique [33, 36]. The scheme of printing continuous fiber-reinforced composites process is provided in figure 2.

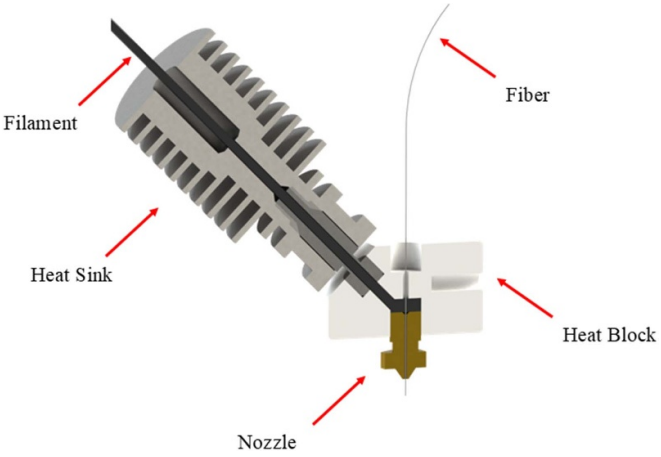

Figure 2. The scheme of printing continuous fiber-reinforced composites based on the simultaneous impregnation technique.

In simultaneous impregnation technique, the glass fiber is impregnated by passing continuously through the melted polymer inside the heated nozzle, after which the composite filament is deposited onto the print bed. During the first stage of printing, a raster composed of impregnated fiber and molten polymer is laid down. Once the polymer cools and solidifies at the starting point, it effectively anchors the fiber to the bed. As the nozzle moves along the printing path and continues feeding the polymer filament, tension is applied to the glass fiber due to this fixed point of the cooled polymer. This tension maintains consistent fiber alignment and ensures that the impregnated fiber is pulled smoothly through the nozzle and accurately deposited along the intended path. In this way, the continuous fiber is fed and laid down in synchronization with the nozzle motion and filament extrusion. The feeding rate of the polymer filament is controlled by the extruder motor, while the tension in the continuous fiber is passively maintained by the movement of the nozzle relative to the anchored starting point of the fiber on the bed. This approach eliminates the need for an active fiber tension system and relies on the coordination of nozzle motion and extrusion speed to achieve proper fiber alignment [34]. In this approach, no additional surface treatment or chemical sizing was applied to improve adhesion between the fiber and the polymer matrix. To enhance the adhesion of the first layer to the printing bed itself, a glue stick was applied to the bed surface, and the bed was heated to maintain sufficient adhesion.

2.2. Samples preparation

In this research, PLA filament with diameter of 1.75 mm was purchased from Esun, China and E- glass fiber yarn was provided by Jiahe Taizhou Co, China. Table 1 represents the material properties of PLA and glass fiber.

Two meta-material designs were investigated. Two parameters were selected as variables in this research,

Table 1. Material properties of PLA and glass fiber.

Parameter	Value
Density of PLA (ρ)	1250 Kg/m^3 [36]
Mass per length	0.1 g m^{-1} [36]
Convection heat transfer coefficient (h_{Conv})	75 $w/m^2\,^\circ C$ [44]
Specific heat capacity of PLA (C)	2060 $j/Kg\,^\circ C$ [45]
Thermal conductivity coefficient of PLA (k)	0.195 [45]
Specific heat capacity of glass fiber (C)	800 $j/Kg\,^\circ C$ [43]
Thermal conductivity coefficient of glass fiber (k)	0.12 $w/m^2\,^\circ C$ [43]
Tensile strength of glass fiber	1000 MPa [34]

Table 2. The list of samples.

Label	Pattern	Volume Fraction (wt%)	Actual Weights (gr)
R0	Re-entrant	0	9.5 ± 0.2
R1	Re-entrant	20	9.8 ± 0.2
R2	Re-entrant	40	10.3 ± 0.5
H0	Hexagonal	0	9.0 ± 0.1
H1	Hexagonal	20	9.3 ± 0.5
H2	Hexagonal	40	10.0 ± 0.1

including the meta-material's pattern (re-entrant and hexagonal) and the volume fraction of glass fiber (0, 20, and 40 wt%). Two common patterns with different applications are selected. The re-entrant was selected as a representative and widely studied auxetic geometry with a negative Poisson's ratio, whereas hexagonal structures offer traditional stiffness and isotropic response. These representative designs enabled clear validation of the process feasibility and capability of new G-code modifier software without introducing additional variables associated with more complex patterns. The chosen fiber volume fractions (0, 20, and 40 wt%) were selected based on a combination of practical considerations and the objective to demonstrate tunability of reinforcement content. Specifically, these values were determined by the printing parameters, including nozzle diameter, fiber diameter, extrusion width, and extrusion multiplier, as well as constraints on print quality and process stability documented in previous studies. Table 2 presents the different samples, their actual weights, and their labels 3D printed to evaluate the effect of pattern and volume fraction on the mechanical properties. The observed weight variations (±0.1–0.5 g) are attributed to normal FDM process dynamics—including extrusion fluctuations during acceleration/deceleration, filament diameter tolerances, and retraction cycles—as well as, in reinforced samples, additional variability from manual fiber feeding and transitions between high- and low-speed printing near edges.

The tensile test samples were 3D printed in a rectangular cuboid shape with dimensions of 200 × 32 × 3 mm according to ASTM D3039M standard. Due to the acceptable failure mode and reasonable frequency, no tabs are applied to the specimens. The three point bending test and compression test samples were 3D printed in a rectangular cuboid shape with dimensions of 45 × 32 × 3 mm and 40 × 32× 10 mm, respectively. As the samples show no slip during the bending test, no support span has been used. Table 3 illustrates the dimensions of different samples according to the mechanical tests.

Table 3. Dimensions of samples for different mechanical tests.

Mechanical test	Dimensions (mm)
Tensile test	200 × 32 × 3
Three point bending test	45 × 32 × 3
Compression test	40 × 32 × 10

Table 4. Printing parameters for manufacturing non-reinforced pure samples.

Parameter	Value
Layer height	0.2 mm
Total number of layers	15
Extrusion width	1 mm
Nozzle diameter	1 mm
Extrusion multiplier	0.97
Nozzle temperature	205 ° C
Bed temperature	55 ° C
Ambient temperature	25 ° C
Printing speed	40 $mm^{-1}\,s$

2.3. 3D/4D printing parameters

The printing parameters of the samples with and without continuous glass fiber reinforcements were selected differently due to the adjustment of fibers in the correct location. The stiffness of glass fiber is much higher than the PLA, and therefore a high printing speed leads to misalignment of fibers at the corners of the parts. To overcome this issue, it is crucial to reduce the printing speed at the corners. Consequently, a G-code modifier software package was developed in this research to automatically detect the edges of the parts and reduce the speed at the edges locally. Table 4 illustrates the printing parameters for pure samples without reinforcement.

The volume fraction of the samples is adjustable by changing the printing parameters such as layer height, extrusion width, and extrusion multiplier. The volume fraction of the parts is defined by the volume fraction of a single printing raster. As is shown in figure 3, the volume fraction can be calculated based on the area of the fiber yarn and total cross section of a raster according to equation (1)

$$Vf = \frac{\pi . D^2/4}{w.h} \tag{1}$$

where the Vf is the volume fraction of glass fiber, D is the fiber diameter, w is the extrusion width, and h is the layer height. This calculation method has been adopted from previous studies [34–36], where it was demonstrated to produce

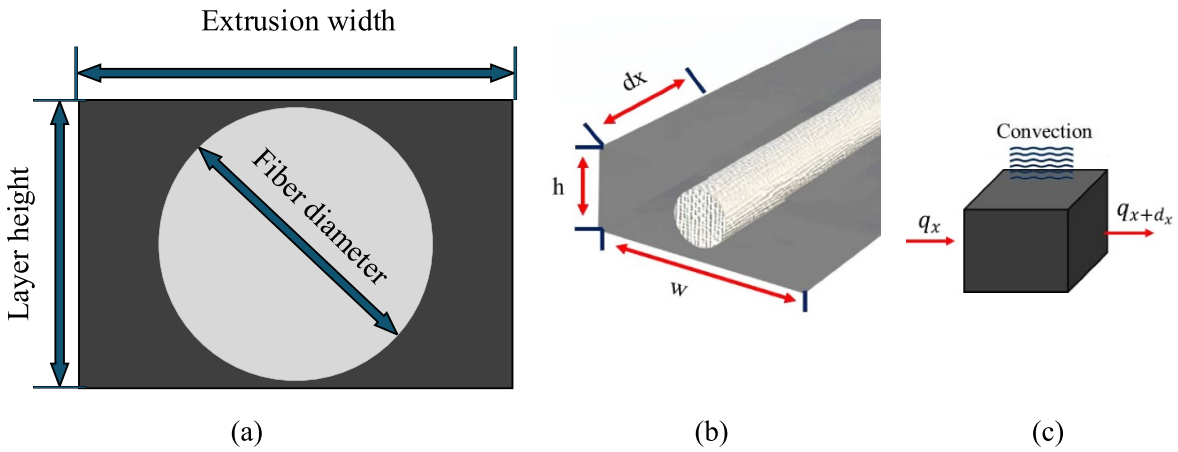

Figure 3. The scheme of a printed reinforced raster (a), its cross section (b) and thermal analyze element (c).

Table 5. Printing parameters of the reinforced composites.

Volume fraction (wt%)	Parameter	Value
20	Layer height	0.3 mm
	Extrusion width	1 mm
	Nozzle diameter	1 mm
	Extrusion multiplier	0.8
	Printing speed of the straight line	40 mm^{-1} s
	Printing speed of the corners	4 mm^{-1} s
40	Layer height	0.3 mm
	Extrusion width	0.5 mm
	Nozzle diameter	0.5 mm
	Extrusion multiplier	0.6
	Printing speed of the straight line	40 mm^{-1} s
	Printing speed of the corners	4 mm^{-1} s

accurate estimates of fiber volume fraction and therefore was applied in this study without further modification.

To enhance the printing quality, it is essential to control the flow of the polymers. If the polymer is deposited more than the demand, the printing quality may decrease and if it is deposited less than demand, the part may not stick to the printing bed. The flow of the polymeric matrix can be adjusted by extrusion multiplier calculated by the following equation

$$\text{Extrusion multiplier} = 1 - Vf. \tag{2}$$

The fiber diameter is constant; therefore, the layer height of the raster is considered constant too. Then, the only variable parameters to achieve desired volume fraction are extrusion width and extrusion multiplier which is a coefficient in commercial slicer software that adjusts the extrusion rate of polymer. Table 5 lists the printing parameters for manufacturing fiber-reinforced composites to achieve for different volume fractions.

2.4. Tool path design

Designing an optimized tool path is essential for successfully printing meta-materials reinforced with continuous fibers due to their complex patterns. A key challenge in this process is eliminating nozzle jumps and non-extruding travels, which are typical in conventional printing but detrimental to continuous fiber placement. For continuous fiber-reinforced composites, the nozzle must maintain uninterrupted extrusion to ensure proper fiber alignment and structural integrity. Figure 4 compares G-codes generated for reinforced and non-reinforced samples using the Prusa slicer. In figure 4(a), the conventional G-code exhibits numerous non-extruding nozzle travels (blue lines), making it unsuitable for continuous fiber-reinforced composites. In contrast, figure 4(b) demonstrates the newly developed G-code, specifically designed to enable continuous extrusion and eliminate nozzle jumps during printing.

To generate a G-code without nozzle jumps or non-extruding travels, two separate paths were designed and subsequently combined to create the final continuous path. Figure 5 illustrates the designed paths for different patterns. Specifically, Path #1 and Path #2 were independently created using CAD software and then imported into the slicing software to generate a new G-code. As shown in figure 5, bridge sections were strategically added to the top and bottom of each path. These bridges ensure a continuous extrusion path and alignment of the start and end points of each segment,

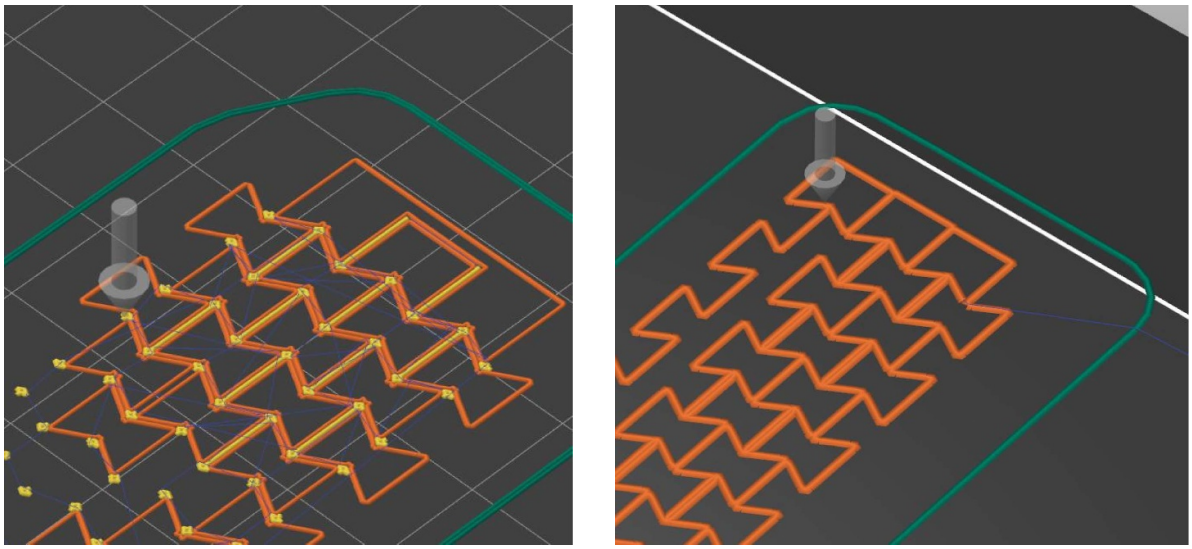

a) b)

Figure 4. Conventional G-code consists of many nozzle jumps and travelling without extrusion (blue lines) (a) and newly developed G-codes generated for printing continuous fiber-reinforced composites without any nozzle jump (b).

enabling seamless printing without interruptions. During the printing of a single layer, the 3D printer first deposits *path #1*, which results in the formation of one half of each cell in the lattice geometry. After completing this path, no fully closed cells exist. To maintain continuous extrusion without interruption, the printer then follows short *bridge sections* that connect the end of path #1 to the start of *path #2*. Once path #2 is deposited, all cells in the layer are fully completed. This sequential approach ensures consistent filament flow and minimizes potential defects related to nozzle retraction and restarting. It should be mentioned that the top and bottom bridges were not the same and different patterns used the unique bridges to avoid any nozzle jumps.

Printing speed poses a significant challenge in fabricating continuous fiber-reinforced composites. High printing speeds can lead to improper fiber alignment, particularly at corners, due to the greater stiffness of the fibers compared to the molten polymer. This misalignment makes it difficult to achieve sharp edges in printed parts [36]. To produce sharp edges, the printing speed must be significantly reduced, allowing the molten polymer to solidify and properly secure the fibers in place. While reducing the overall printing speed through slicing software is possible, it results in prolonged printing times. To address this issue, a G-code modifier software package was developed based on LabView programming language in this research. This software identifies the edges of 3D models and selectively reduces the printing speed at the edges, maintaining a higher speed for straight-line segments. Figure 6 illustrates the graphical user interface (GUI) of the G-code modifier software. The software operates in two main stages. In the first stage, the printing parameters for composite samples are calculated based on equations (1) and (2). In the second stage, edge recognition and G-code modification are performed to optimize the printing process.

After developing an initial G-code with no nozzle jumps during printing, the file was imported into the custom G-code modifier software to optimize edge-specific printing speeds and create a modified G-code so-called compo-code for 3D/4D printing. This software reduces the printing speed at the edges, where the nozzle path changes abruptly, ensuring proper fiber placement and part quality. The compo-code generated by the software incorporates these adjustments, enabling precise printing at critical points. Figure 7 compares the original and compo-codes, clearly demonstrating the reduction in printing speed at the edges locally.

2.5. G-code modifier software logic

The newly developed G-code modifier software identifies the edges of parts directly from the original G-code rather than the STL file. When a CAD file is converted to an STL format, it is represented as numerous triangular meshes, causing curves in the design to be approximated by a series of small straight segments. Figure 8 illustrates the STL file of the re-entrant pattern. Typically, commercial slicers output G-code containing only the G01 and G00 commands, which are used for moving along straight-line paths. Unlike CNC machines, they do not include G02 and G03 commands for circular interpolation. The slicing software generates a G-code line for each of small segments that interpolate the curves when printing curves, as well as for long straight lines. Each time the nozzle changes its path, a new G-code line is created. As a result, the generated G-code contains thousands of lines describing individual straight segments. Each line specifies the coordinates of the endpoint of a straight path, while the preceding line defines the start point of that segment.

These straight-line segments can be classified into two categories:

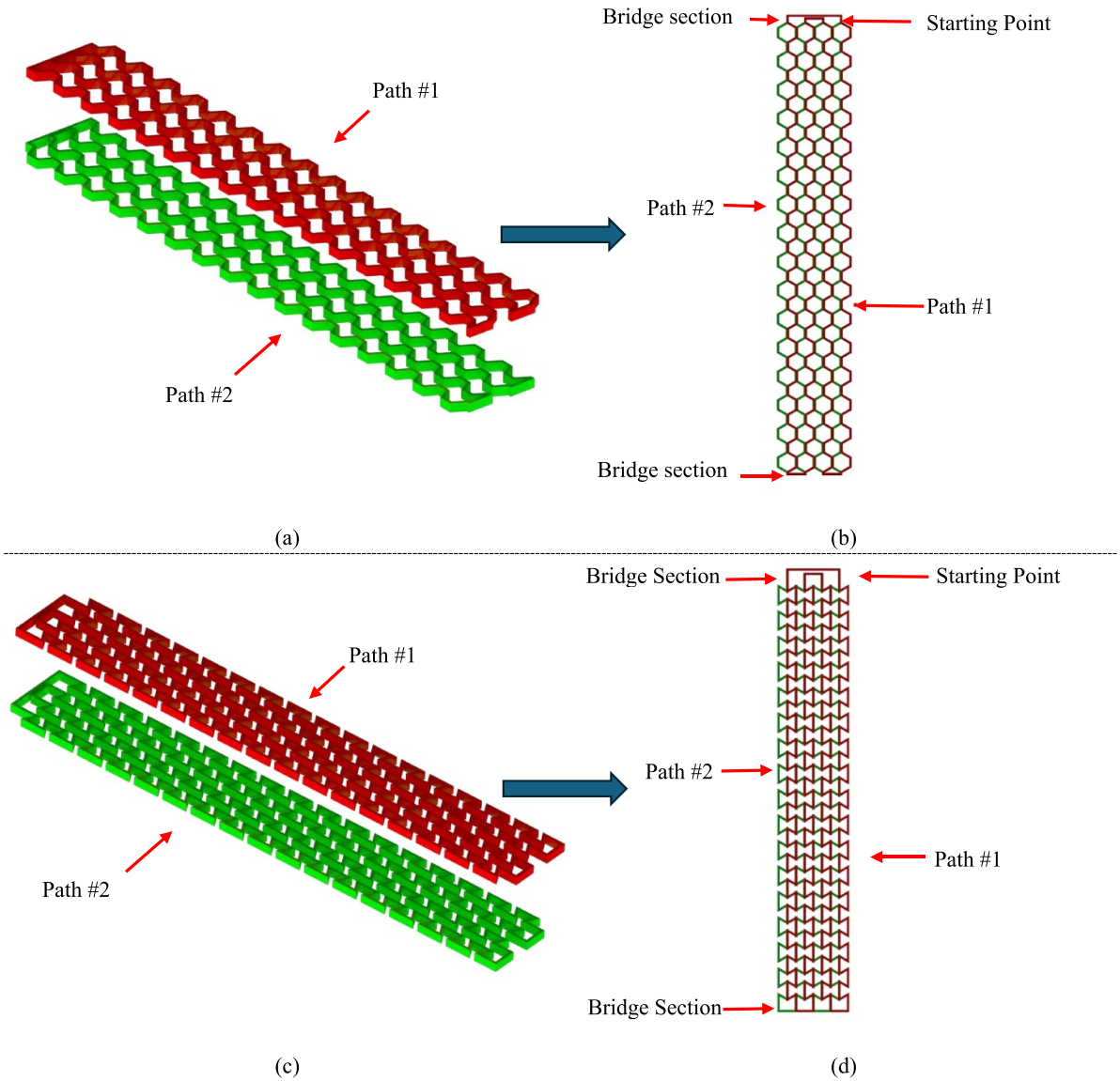

Figure 5. Two separately designed paths (a) to create a hexagonal patterned meta-material (b). Two separately designed paths (c) to create a re-entrant patterned meta-material (d).

- *True straight lines*, which represent actual straight edges in the geometry of the printed part.
- *Approximation lines*, which are short segments used to approximate curves.

To distinguish between these categories, the software defines an *edge recognition value* (figure 6(b), #1), specified by the user. The algorithm iteratively calculates the coordinates of each segment's start and end points, computes the angle between consecutive segments, and measures the length of each line. If the length of a segment is less than the edge recognition threshold, it is classified as an approximation line; otherwise, it is considered a true straight line.

For approximation lines (curved regions), the software reduces the printing speed across the entire segment. Specifically, it multiplies the original feed-rate by the user-defined *speed reduction percentage* (figure 6(b), #2) and appends the adjusted feed-rate to the corresponding G-code line. For example:

- Original G-code:
  G01 X… Y… E… F100
- Modified G-code with 10% speed:
  G01 X… Y… E… F10

For true straight lines, the software further refines speed control by introducing deceleration zones at the beginning and end of each segment. Based on the angle between the preceding and following lines, the program generates two new shorter lines before and after the original segment, defined by a user-specified *edge shift back distance* (figure 6(b), #3). Reduced speed is applied only within these short transition

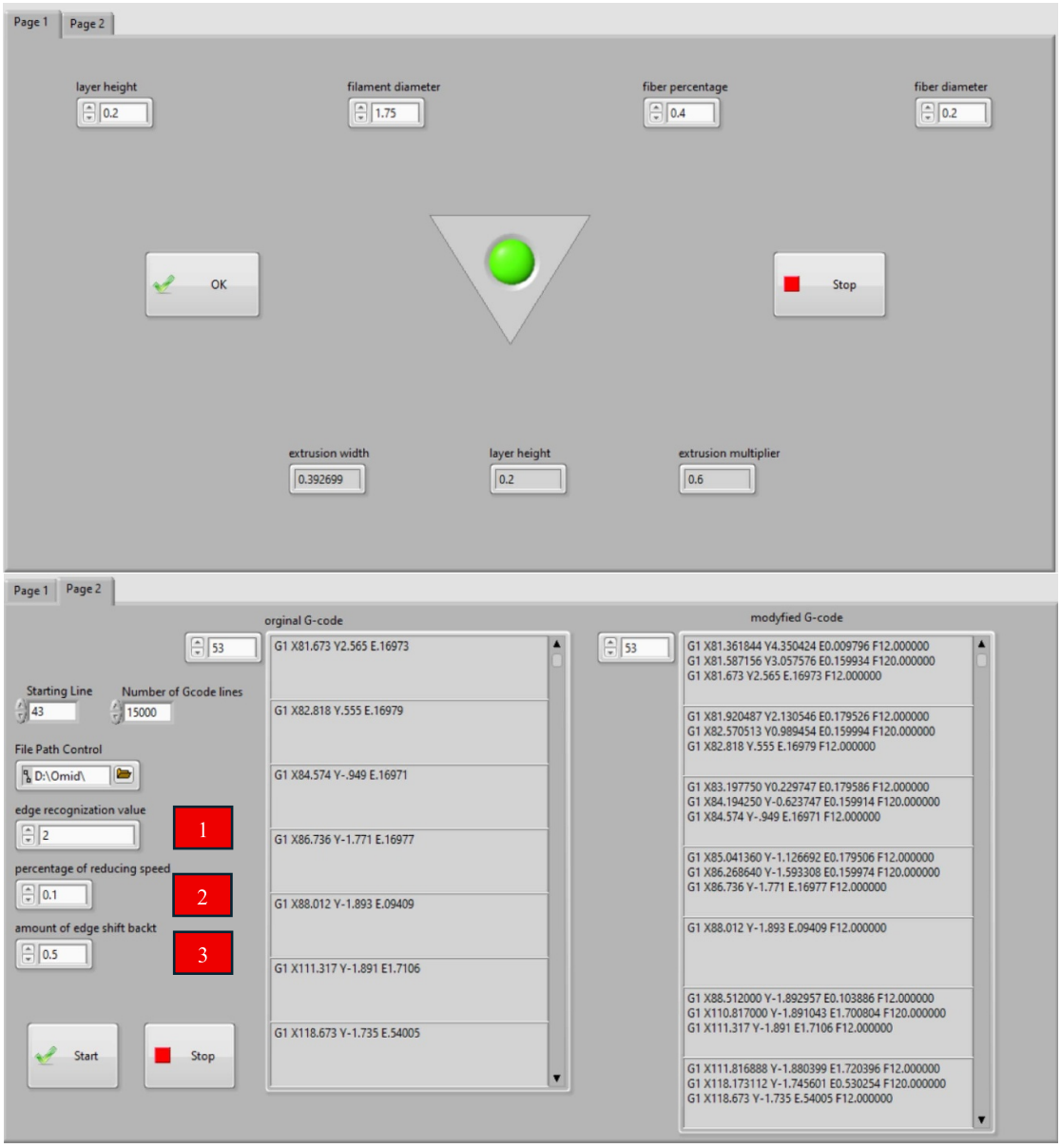

Figure 6. The first (a) and second (b) pages of the newly developed G-code modifier software.

lines, allowing the nozzle to traverse the central portion of the straight path at the original feed-rate. For example, consider two consecutive straight-line G-code commands:

- Original G-code:
  G01 X10 Y0 E… F100
  G01 X10 Y10 E… F100
- Modified G-code with an edge shift back of 1 unit and 10% speed reduction:
  G01 X9 Y0 E… F100
  G01 X10 Y0 E… F10
  G01 X10 Y1 E… F10
  G01 X10 Y9 E… F100
  G01 X10 Y10 E… F10

This approach ensures that speed is selectively reduced near edges and curves, improving deposition accuracy while maintaining higher feed-rates along straight paths.

Figure 9 illustrates the algorithm implemented in the G-code modifier software, demonstrating how edges and curves are identified and optimized for improved printing performance to generate compo-code.

The algorithm implemented in the G-code modifier software enables it to accurately detect edges in parts with any geometry. Additionally, the software can identify the edges of infill patterns, ensuring comprehensive optimization of the printing process. Based on the algorithm, it should be noted that the performance of the edge recognition algorithm depends on the resolution of the STL mesh used to generate the

(a)

(b)

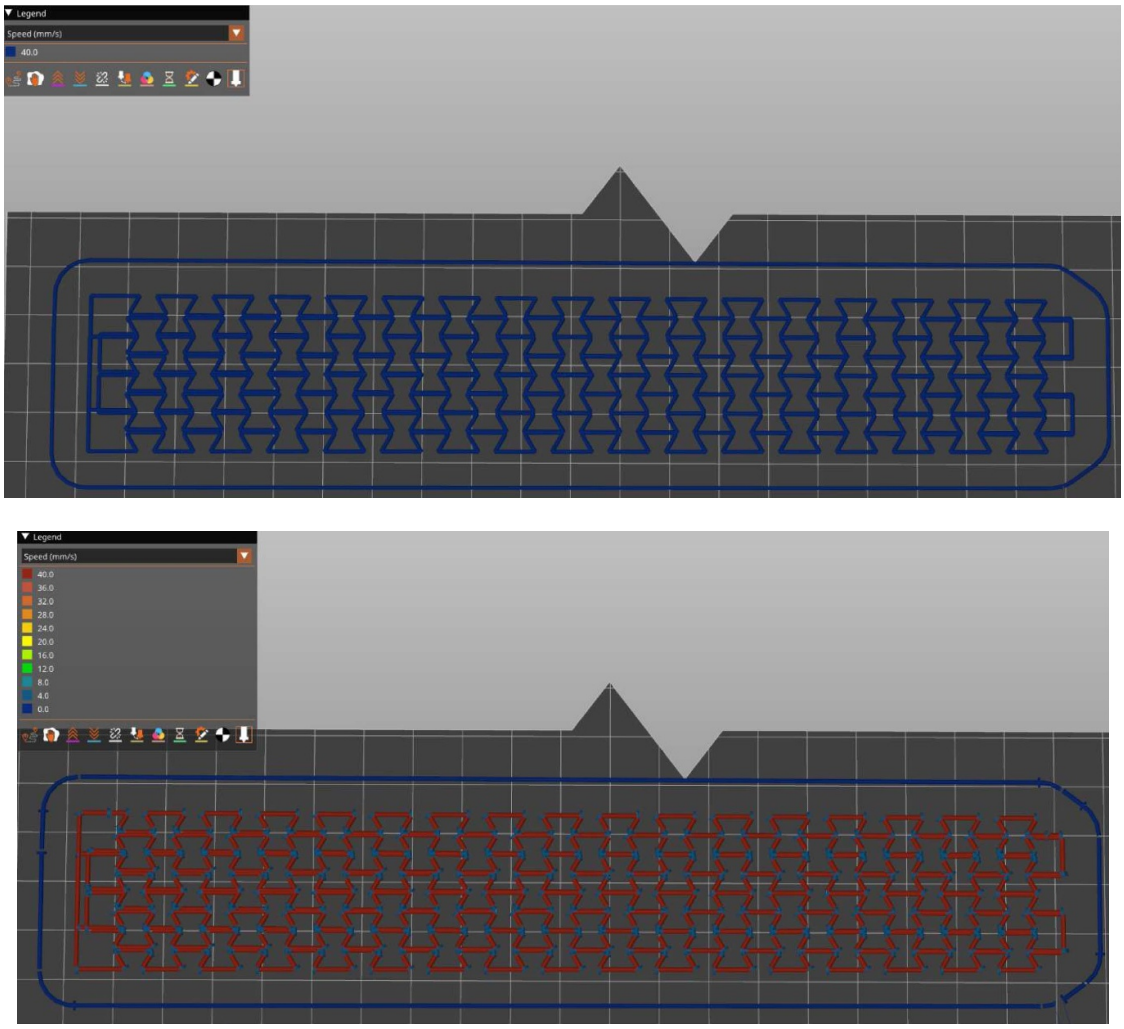

Figure 7. Original G-code (a) and compo-code (b) for 3D printing a re-entrant patterned meta-material.

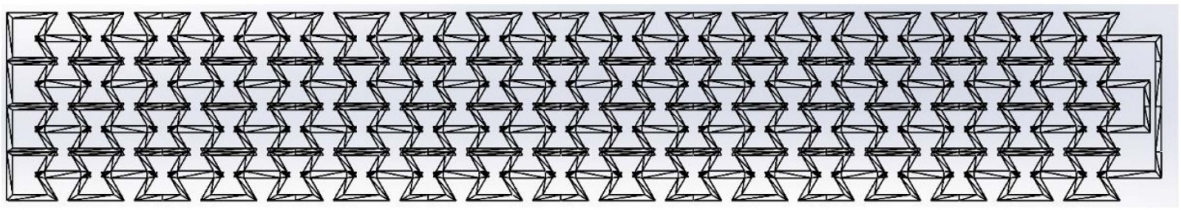

Figure 8. The STL file of the re-entrant patterned meta-material.

original G-code. High-resolution meshes yield a greater number of short segments approximating curves, requiring appropriate adjustment of the edge recognition value. Figure 10 illustrates the capability of presented algorithms to detect the different features such as curves and sharp edges that cause the misalignment of fiber. Figure 10 demonstrates a printing speed comparison between the original G-code and compo-code, highlighting the enhanced edge detection and optimized printing parameters. Print time reduction can be estimated by calculating the cumulative length of edges and curves printed at reduced speed and applying the corresponding speed differences. This functionality is not yet integrated into the software but will be considered for future development.

Based on equations (1) and (2), the desired volume fraction of glass fiber can be achieved by modifying three key parameters: layer height, extrusion width, and extrusion multiplier. Since the layer height remains constant due to the fixed diameter of the glass fiber, the primary adjustable variables are the extrusion width and extrusion multiplier. Reducing the extrusion width from 1 mm to 0.5 mm effectively doubles

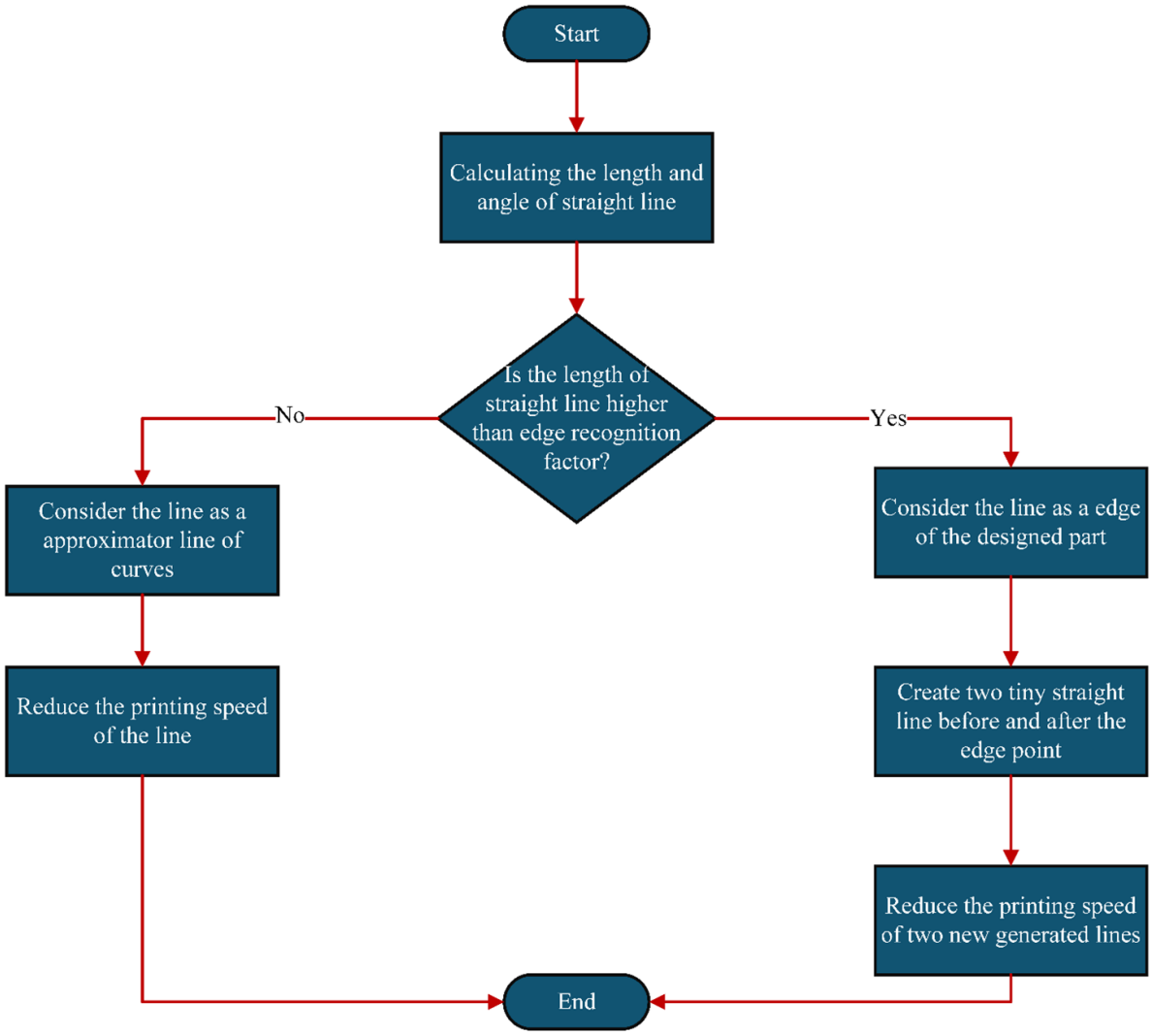

Figure 9. The algorithm of G-code modifier software.

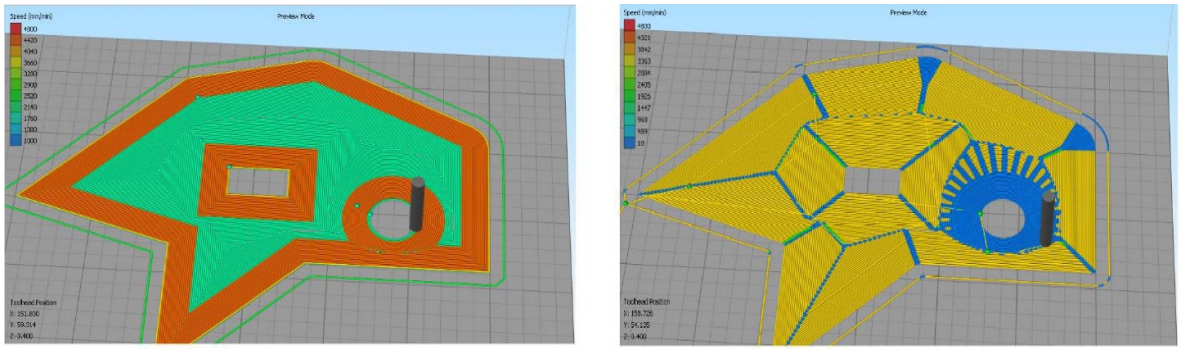

(a) (b)

Figure 10. The printing speed of the original G-code (a) and compo-code (b) using the G-code modifier software.

the volume fraction of the printed parts. During this process, the nozzle extrudes two rasters to form a single line, ensuring uniform fiber distribution. Figure 11 illustrates the extrusion widths for samples with 20 wt% and 40 wt% glass fiber volume fractions.

2.6. Heat transfer

The best printing speed of continuous fiber reinforced composites is the one which allows partial part of the polymer to cool down to below the glass transition temperature (Tg) before printing the edges or curves are finished. Therefore, it is

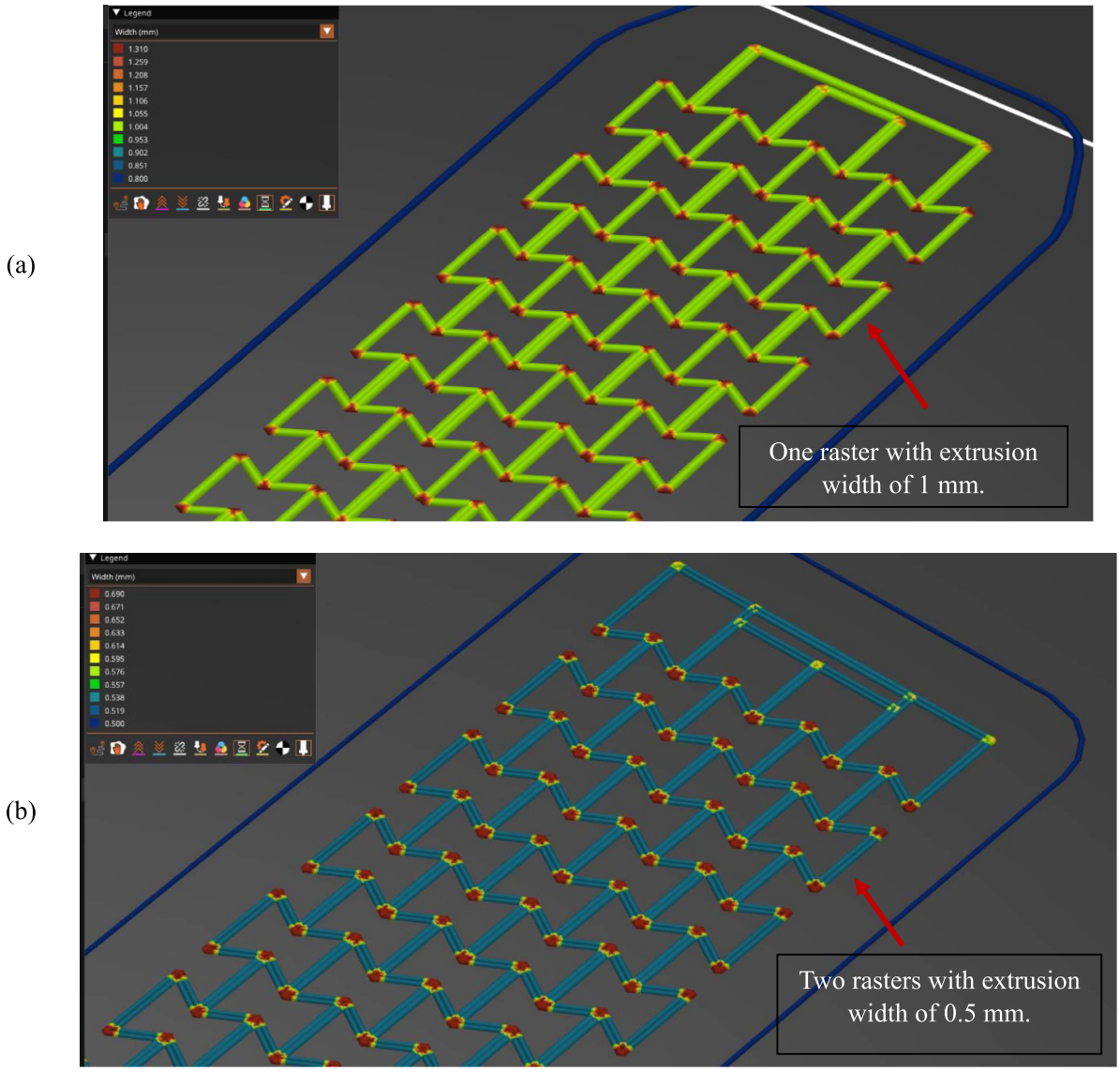

Figure 11. The G-codes of 3D printing composite sample with (a) 20 wt% and (b) 40 wt% of the glass fiber.

essential to analyze heat transfer in the FDM process. Figure 4 shows a raster of a defined length is being deposited onto the bed and an element is selected to compute the temperature at various locations through thermal analysis. It is assumed that the cross-section of both the element and the deposited raster resembles a rectangle. Consequently, the rounded corners of the raster are not considered in analyzing, as they do not significantly affect the cross-sectional dimensions and analysis. The heat transfer from the printed raster to the bed was neglected, as the bed temperature (approximately 55 °C) was only slightly above ambient temperature and primarily affected the first layer. As additional layers are deposited, the relative influence of bed conduction decreases. It is assumed that the heat transfer is one-dimensional along the x-axis and that the coordinate origin is at the nozzle output and the element length is equal to dx [36, 46]. This simplification facilitates analytical tractability. However, it is acknowledged that the rounded corners introduce localized variations in surface area and convective heat loss, which may lead to slight discrepancies between the model predictions and the actual temperature distributions, particularly near the filament edges. The first law of thermodynamics states that the heat transfer from the element's bottom to its bed (or previous layer) is equal to the heat transfer caused by convection from the surroundings:

$$q_x - q_{x+d_x} - h_{\mathrm{Conv}} A_{\mathrm{Conv}} \left(T - T_\infty\right) = \rho C V \left(\frac{\mathrm{d}T}{\mathrm{d}t}\right) \qquad (3)$$

where T and T_∞, A_{Conv}, and h_{Conv} represent the temperature of the specimen at a specific point in time, the ambient temperature, the convection heat transfer coefficient, and the sections that are in contact with the environment, respectively. q_{x+d_x} and q_x are respectively the output conduction heat transfer from the element and the input conduction heat transfer from the element. ρ, C, V, and $\left(\frac{\mathrm{d}T}{\mathrm{d}t}\right)$ represent density, the specific

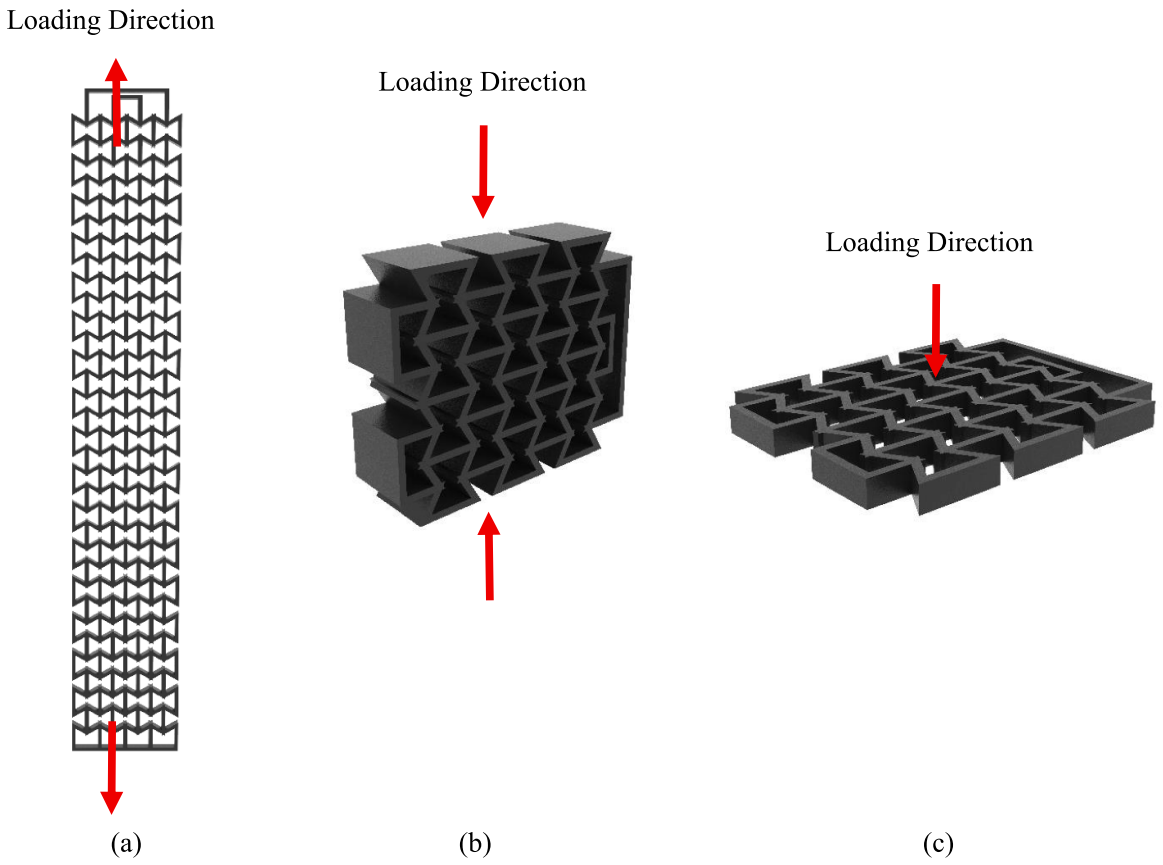

Figure 12. Loading direction of tensile test (a), compression test (b), and three-point bending test (c).

heat capacity, the volume of the element, and the temperature change over time, respectively.

By assuming the temperature at $x = 0$ equals the nozzle temperature (TN) and layer height is equal to the fiber diameter, the solution to equation (3) for temperature at a specific distance from the nozzle is obtained as [36, 46]:

$$T(x) = (T_N - T_\infty)\, e^{\left(\frac{x}{2}\right)\left(a-\sqrt{a^2+4b}\right)} + T_\infty \tag{4}$$

$$a = \frac{\rho C \nu}{k} \tag{5}$$

$$b = \frac{2h_{\mathrm{Conv}}\,(h+w)}{k\left(wh - \left(\frac{\pi}{4}\right)d_f^2\right)} \tag{6}$$

where k and ν represent and conduction heat transfer coefficient and printing speed, respectively.

2.7. Mechanical properties

Mechanical properties of the fiber-reinforced composites in various modes such as tensile, compressive, and flexural strength were evaluated according to ASTM D3039M, ASTM D695, and ASTM D790, respectively. A universal testing machine with a load cell capacity of 20 kN was used to evaluate the mechanical properties. Crosshead displacement speed was adjusted to 5, 3, and 3 mm min $^{-1}$ for tensile, compressive, and three-point bending tests, respectively. Figure 12 demonstrates the loading direction for different tests.

2.8. Shape memory behavior

To investigate the shape memory behavior of the fiber-reinforced composites under different mechanical loading conditions (bending and compression) and cold programming method, two different tests were conducted. To investigate the shape memory behavior of samples under compression loading conditions, the samples with dimensions of 40 × 32 × 10 mm were programmed in a compression mode with a displacement of 15 mm and loading rate of 3 mm min^{-1}. The samples experienced loading and unloading and then were heated in a container full of 70° C water for shape recovery. Finally, the samples were cooled to the lab temperature (22° C) and then their height was measured by a digital caliper. To analyze the shape memory behavior of samples under bending loading conditions, the samples with dimensions of 45 × 32 × 3 mm were programmed via a three-point bending loading-unloading with a maximum displacement of 6 mm and loading rate of 3 mm min^{-1}. After loading and unloading, the samples were heated in a container full of 70° C water for shape recovery. Finally, Images were taken before and after heating the samples by Microscope (Dino-Light Premier,

AnMo Electronics, Taiwan), and the shape recovery angle was measured by Dino Capture 3.0 software.

2.9. Statistical analysis

All mechanical and shape-memory tests were conducted on five samples, to calculate standard deviation (SD) and achieve reliable result. Force–displacement curves represent a typical specimen from each group. Due to variability in displacement behavior among samples, statistical analysis was performed on peak force, and energy absorption values. A two-sample t-test (Minitab16 software) was implemented for statistical analyses. A p-value < 0.05 was considered significant. SD and mean were calculated and used to present all experimental data in the following section.

3. Results and discussion

In this section, meta-materials 3D/4D printed via the compo-code are demonstrated and their mechanical and shape-memory properties such as tensile strength, compression strength, bending strength, shape recovery and energy absorption capabilities are investigated.

3.1. Calculating printing speed

When the nozzle starts printing a straight line from the starting point to the endpoint, the polymer at the starting point must cool below the glass transition temperature before the nozzle reaches the endpoint. This ensures that the fiber is properly positioned and remains fixed in place when the nozzle changes direction. The smallest length of a straight line in the re-entrant and hexagonal pattern is about 10 mm, so the best printing speed is the one that causes the temperature drop down below the glass transition of PLA (about 80 °C [36]) in 9 mm. The solution of equation (4) by using the values of tables 1, 4, and 5 for printing speed of 40 mm s^{-1} and 4 mm s^{-1} are presented in equations (7) and (8) respectively:

$$T(x) = 180e^{-0.0103} + 25 \tag{7}$$

$$T(x) = 180e^{-0.1036} + 25. \tag{8}$$

Figure 13 illustrates the temperature reduction for two different printing speeds (4 mm s^{-1} and 40 mm s^{-1}), calculated using equations (7) and (8). As shown in the figure, at a printing speed of 4 mm s^{-1}, the temperature drops below the glass transition point within 10 mm. This allows for proper fiber alignment, as the minimum feature length of each metamaterial pattern is approximately 10 mm. It should be noted that equations (7) and (8) are scalable and can be re-parameterized for different pattern sizes, extrusion widths, layer heights, and printing speeds by adjusting the extrusion widths, layer heights, and travel distance (x) and incorporating updated process parameters into equations (6) and (4). This flexibility enables the cooling model and G-code modification strategy to be applied to a wide range of design geometries and printing conditions.

3.2. Lattice printing methods

The newly developed G-code modifier software was implemented to increase the accuracy of latticed meta-material printing. The G-code modifier software decreases the printing speed at the edges to enhance the accuracy of continuous fiber-reinforced parts. Figure 14 demonstrates two re-entrant meta-materials one of which was printed by the compo-code and another one was printed by a common G-code. As shown in figure 14(a), the fibers were located properly in samples printed by the compo-code. However, the fibers were not located at right positions when printing by the common G-code, especially at the corners, see figure 14(b). There is a gap between fibers in samples printed by the common G-code and the fibers tend to move inside the re-entrant cell due to the printing path. However, no gap is seen in figure 14(b) between fibers of samples printed with the compo-code.

It is worthwhile to mention that it would be possible to print continuous fiber-reinforced composites with low printing speed to achieve high accuracy, but the printing time increases dramatically. Table 6 illustrates the accuracy and printing time of the re-entrant pattern with 20 wt% of glass fiber and different G-codes. It is found from table 6 that using the compo-code results in high accuracy with less printing time. It reveals the importance of the new G-code modifier software for printing continuous fiber-reinforced composites. 'High Accuracy' was determined qualitatively by comparing the printed pattern to the original CAD geometry, assessing fiber alignment accuracy, consistency of raster deposition, and the absence of visible defects such as gaps, over-extrusion, or fiber misalignment.

3.3. Tensile tests

Figure 15 shows the tensile force-displacement response of the meta-composites with re-entrant pattern with different glass fiber volume fractures and G-codes (Compo-code and common G-code). As shown in figure 15, the tensile strength of samples printed using the Compo-code increased slightly by approximately 8% due to improved fiber alignment. Additionally, this increment was expected due to the previous researches which show that reducing the printing speed results in higher tensile strength [47]. The Compo-code achieves this by decreasing the printing speed at the edges-locations where residual stress typically occurs.

Figure 16 demonstrates the tensile force-displacement response of the meta-composites with different glass fiber volume fractures and patterns. Figure 16 clearly illustrates an increase in tensile strength when volume fracture of glass fiber increases and results are consistent with the rule of mixture shown in equation (9)

$$\sigma_c = V_f.\sigma_f + (1 - V_f).\sigma_m \tag{9}$$

where σ_c is composite tensile strength, σ_f is fiber tensile strength, σ_m is matrix tensile strength and V_f is volume fraction. The tensile strength of non-reinforced parts with a re-entrant pattern is higher than samples with a hexagonal pattern. On the other hand, the tensile strength of reinforced

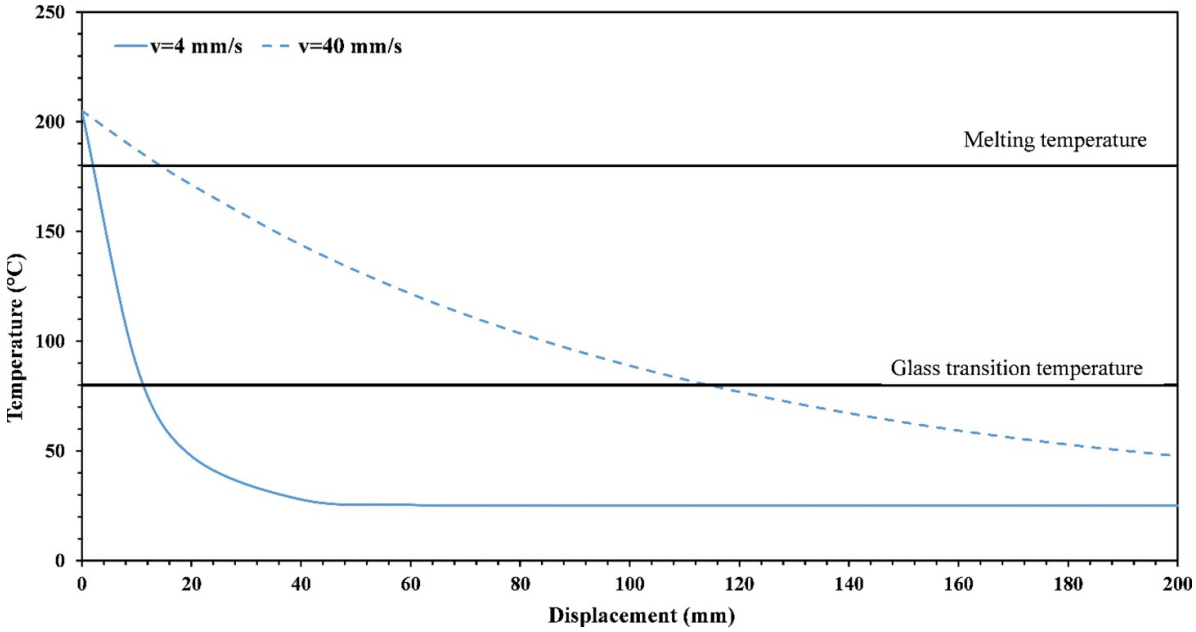

Figure 13. Temperature reduction according to nozzle travel for different printing speeds.

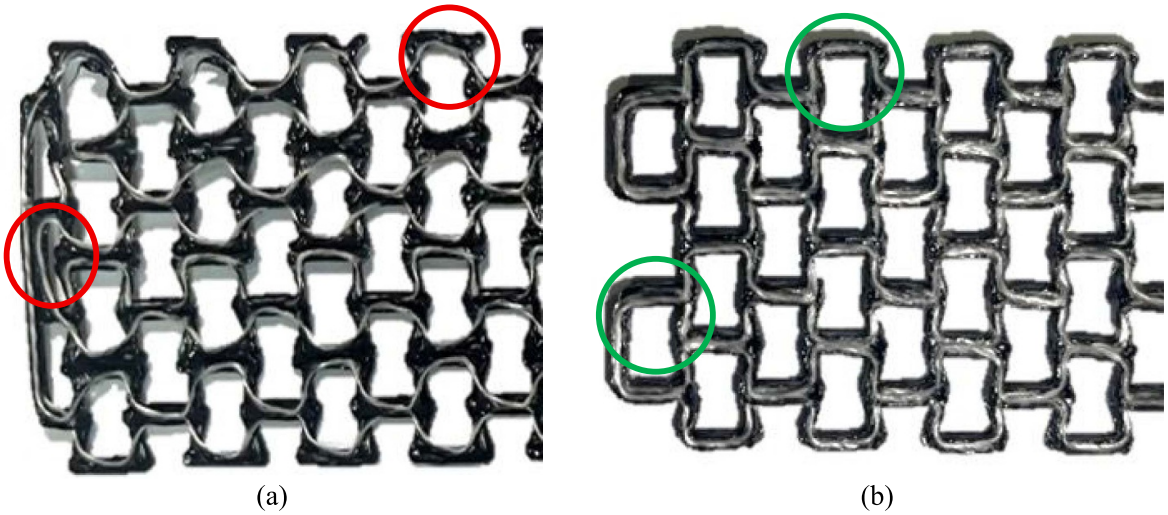

Figure 14. Re-entrant meta-materials printed with (a) common and (b) modified G-codes.

Table 6. Printing time of the whole parts and accuracy of different samples printed with high, low, and modified printing speeds.

G-code Type	Printing Speed	Accuracy	Printing Time
Common	40 mm s^{-1}	Low	18 min
Common	4 mm s^{-1}	High	137 min
Compo-code	40 mm s^{-1} for printing the straight line and 4 mm s^{-1} for printing the edges	High	85 min

samples with a hexagonal pattern is higher than the re-entrant samples. It may be due to stress concentration in the corners of the re-entrant pattern. Figure 16 shows that the sample with a hexagonal pattern and 40 wt% of glass fiber reaches the maximum force of 2614 ± 96 N and a failure displacement of 25 mm. The hexagonal pattern shows the higher tensile strength while the re-entrant pattern shows the higher failure displacements of 27 and 38 mm for non-reinforced and reinforced samples. Figure 16 also clearly demonstrates that increasing the percentage of glass fiber makes the samples stiffer. The reinforced hexagonal pattern shows a higher stiffness than the re-entrant pattern under tensile loading due to the orientation of fibers. In addition, a quasi-constant force region can be seen in non-reinforced samples according to

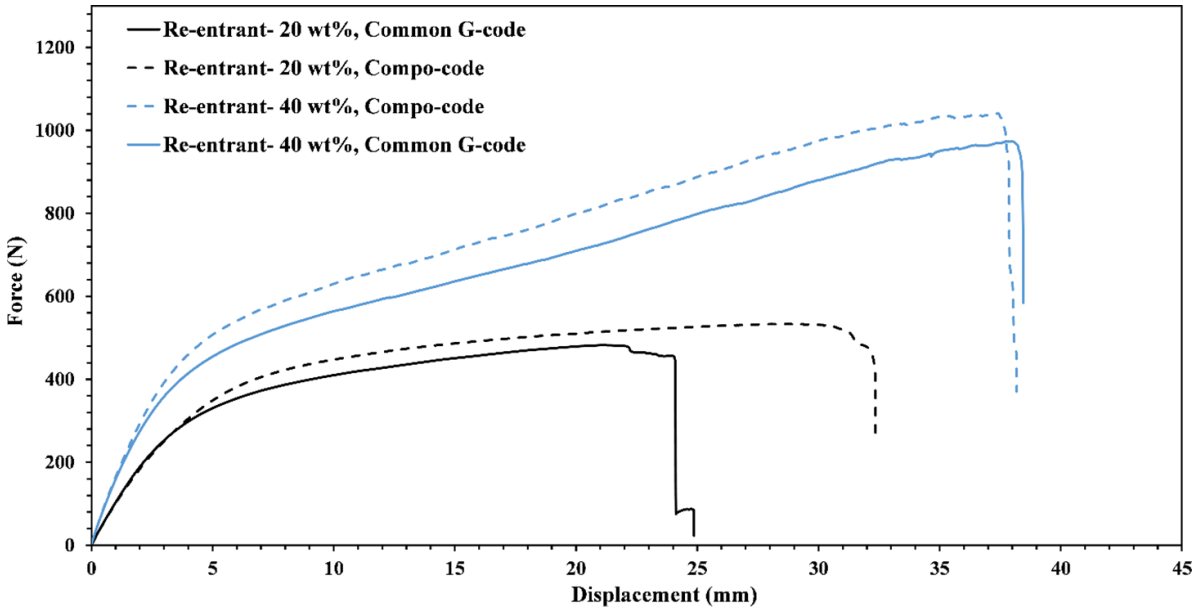

Figure 15. The tensile force-displacement response of reinforced re-entrant meta-materials with different glass fiber volume fractions and G-codes.

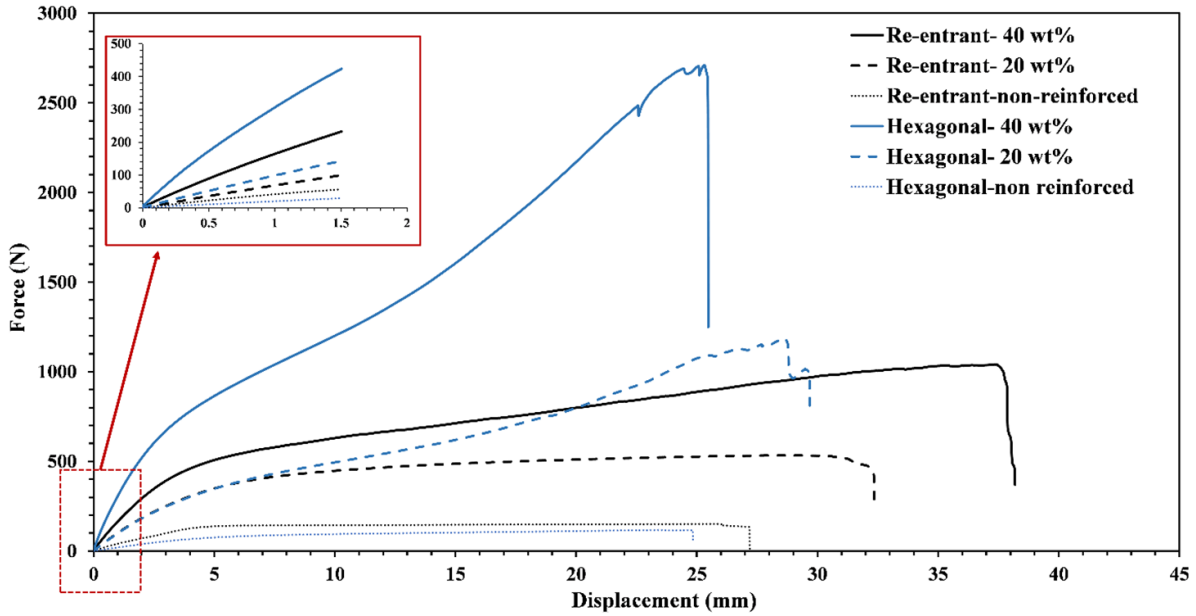

Figure 16. The tensile force-displacement response of reinforced and non-reinforced meta-materials with different patterns and glass fiber volume fractions.

figure 16, where force remains approximately constant over a range of displacements before failure. Re-entrant pattern shows a wider quasi-constant force region than hexagonal pattern due to the auxetic nature of re-entrant structure which promotes stress distribution in structure. Therefore, it causes minimum amount of stress concentration and structure can deform locally over a range of displacements without an increase in force. Reinforced hexagonal pattern shows no quasi-constant force region due to parallel loading with fibers that leads to carrying the loads effectively by the fibers. This type of fiber orientation causes a highly resistance configuration to the deformation. On the other hand, the quasi-constant force region can be observed in reinforced re-entrant pattern with higher force plateau than non-reinforced samples.

Figure 17 demonstrates the fracture mode of non-reinforced and reinforced (40 wt% fiber) meta-materials under tensile loading. As can be seen in figure 17, the fracture at samples with a re-entrant pattern occurs at the corners and the samples fail from the sharp edges. In addition, the orientation of fibers is one of the main reasons for the lower tensile strength of re-entrant patterns. The strength of the transverse lines in re-entrant patterns is much lower than longitudinal tensile

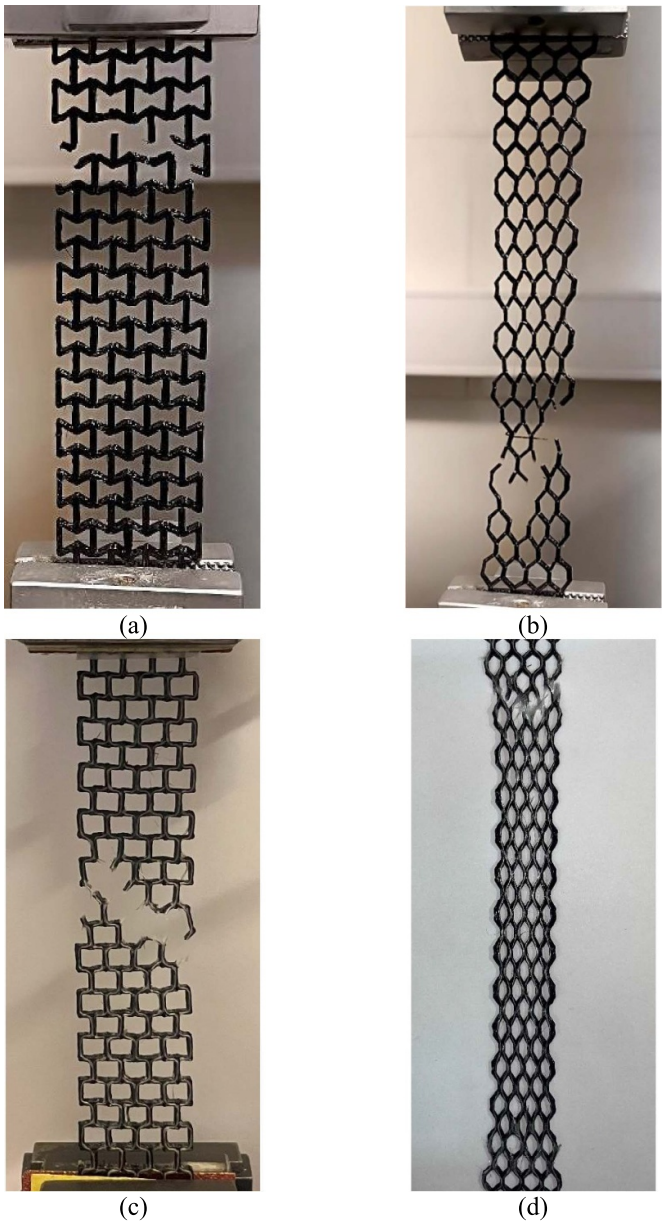

Figure 17. The failure configuration of non-reinforced (a), (b) and 40 wt% fiber-reinforced (c), (d) meta-materials with (a), (c) re-entrant and hexagonal (b), (d) patterns.

strength because the matrix material, which is weaker than the fibers, primarily resists the load in this direction. On the other hand, fibers and loading are parallel approximately in a hexagonal pattern and this causes the highest tensile strength for most fiber-reinforced composites as the fibers carry the majority of the load.

3.4. Compression tests

Figure 18 demonstrates the compressive force-displacement response of meta-materials with different fiber volume fractions and patterns and the densification point of each sample. In contrast to the tensile test, it is observed that the re-entrant pattern has a higher compression strength than the hexagonal pattern for all cases. The re-entrant pattern with 40 wt% of glass fiber has the highest compression strength before the densification phase. As illustrated in figure 18, the auxetic structure contracts in both longitudinal and transverse directions under vertical mechanical loading. Specifically, as the external indenter applies additional compression to the meta-structure vertically, the auxetic design also contracts laterally. This causes the material to flow toward the collision area, resulting in a denser structure with enhanced resistance to collisions. This characteristic influences the force-displacement curve, where a localized hardening effect (local densification) is observed. Figure 18 exhibits that the re-entrant pattern with 40 wt% of glass fiber reaches a maximum force of 360 N before the densification phase starts at 18 mm of displacement. Figure 18 clearly demonstrates that the non-reinforced hexagonal pattern experiences multiple local densifications at 8, 12 and 18 mm of displacement, but the densification of other samples starts approximately around 18–20 mm of displacement. Because there is no reinforcement in non-reinforced hexagonal lattices, the cell walls cannot tolerate significant force and deform easier locally. Multiple densifications begin earlier because of this early collapse. The reinforced and non-reinforced hexagonal samples lack the re-entrant design's inward-slanting walls. Under compressive loads, its cell walls are more likely to flex or collapse uncontrollably. Because the hexagonal structure does not possess auxeticity to prevent deformation, it achieves lesser force resistance in compression. The reinforced re-entrant pattern shows an extended quasi-constant force plateau which shows a great steady energy absorption capability by local deformation of structure before densification phase. In contrast, the hexagonal pattern demonstrates a lower quasi-constant force level. Generally, increasing volume fraction of glass fibers leads to an extended and stable quasi-zero stiffness regime and a more consistent force plateau while non-reinforced samples show a lower and shorter quasi-constant force range due to lower stiffness and earlier start of densification.

3.5. Three-point bending tests

Figure 19 illustrates the three-point bending force-displacement behaviors of meta-composites with different fiber volume fractions and patterns. Figure 19 reveals that the hexagonal pattern always results in a higher bending strength than the re-entrant pattern due to the fiber orientation of the hexagonal pattern. A similar trend was observed for the meta-composites under tensile loading as presented in figure 16. The impact of the glass fiber volume fraction on the bending performance seems very less significant compared to the pattern's effect. For instance, re-entrant meta-composites with 20 and 40 wt% of glass fiber have a very similar behavior under bending. It is also the case for hexagonal patterns till 3 mm of displacement after which the one with 20 wt% of glass fiber experiences a drop in force. The hexagonal pattern with 40 wt% of glass fiber reaches the maximum force of 196 ± 18 N. On the other hand, the re-entrant pattern reaches the maximum load of only 56 ± 6 N. It is worthwhile to mention that all samples experience plastic deformation during

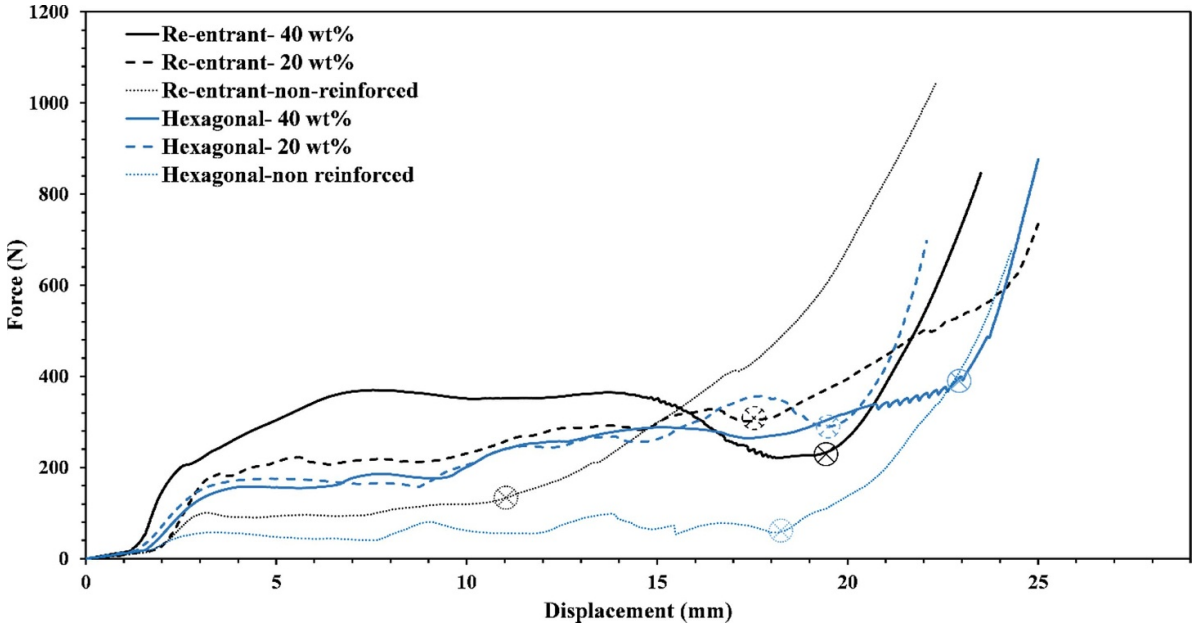

Figure 18. The compressive force-displacement response of meta-materials with various fiber volume fractions and patterns.

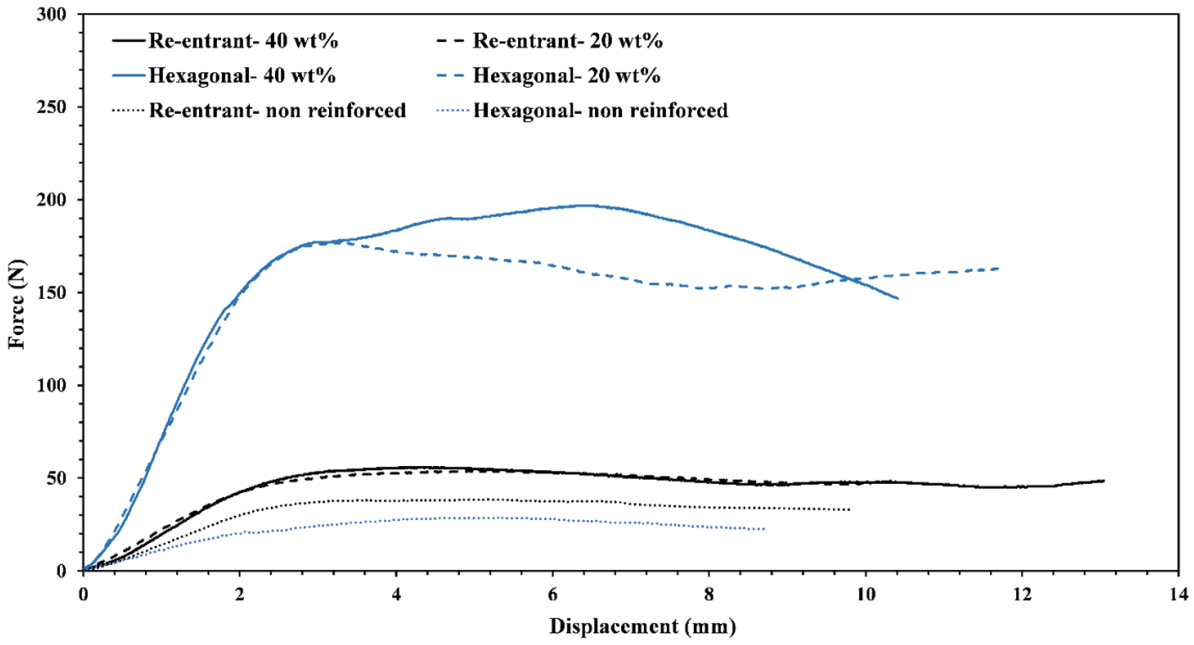

Figure 19. The three-point bending force-displacement of meta-materials with different fiber volume fractions and patterns.

loading. The quasi-constant force plateau can be seen in all samples. The reinforced re-entrant shows a more stable plateau region with a lower force level than reinforced hexagonal pattern. It is the result of a more efficient load transfer mechanism to the fibers in hexagonal pattern. Figure 19 clearly shows reinforcing the samples with continuous glass fibers leading to extended quasi-constant force plateau.

The mechanical hysteresis of meta-composites, identified as noncoincident loading-unloading curves, is further investigated via mechanical loading up to 6 mm displacement and then unloading to zero force. Figure 20 shows the bending hysteresis loop of meta-composites with different fiber volume fractions and patterns. The meta-structures partially recover their original shapes while a residual plastic deformation around 2.7 mm remains into the material and meta-structure at the end of unloading stage. The external force's input energy is converted to kinetic energy, and part of it is dissipated through the mechanism of the plastic deformation. The mechanical hysteresis loop shows all the energy dissipation via two mechanisms of the plastic deformation and buckling-type instability. Figure 20 demonstrates that a higher level of external force is dissipated by the hexagonal design, resulting

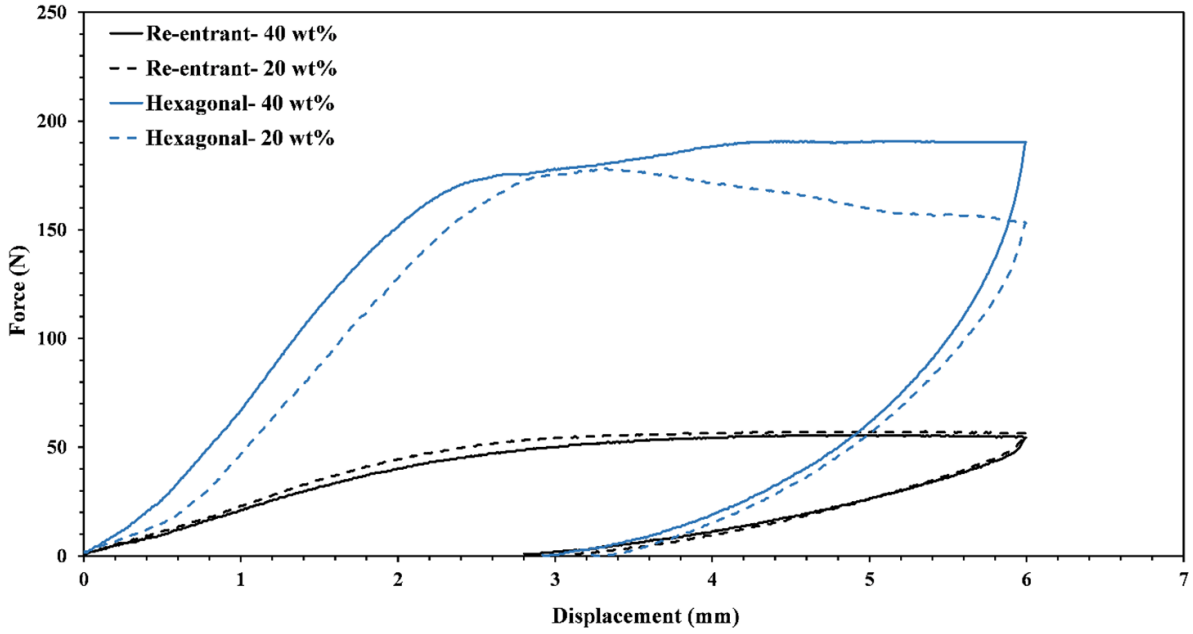

Figure 20. The bending hysteresis force-displacement response of meta-composites with different fiber volume fractions and patterns.

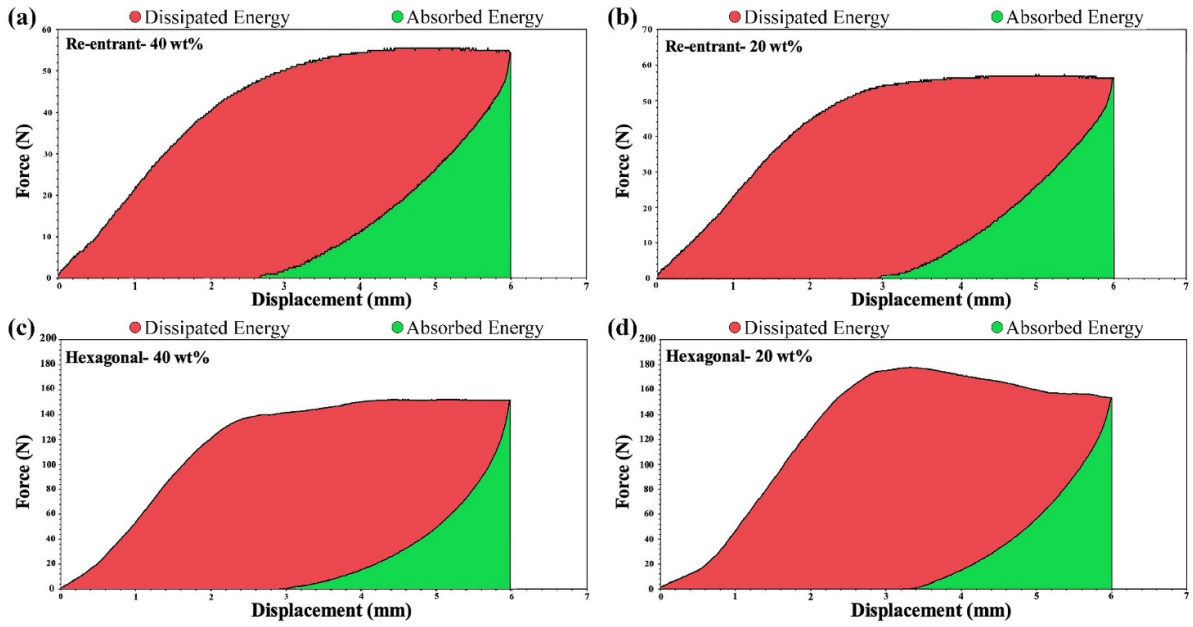

Figure 21. The loading-unloading force-displacement path with dissipated and absorbed energies highlighted in red and green for the meta-composites with re-entrant (a), (b) and hexagonal (c), (d) patterns and 20 wt% (b), (d) and 40 wt% (a), (c) of glass fiber.

in larger energy dissipation and absorption during the loading-unloading cycle.

The energy dissipation and energy absorption capabilities of meta-composites investigated in figure 20 is further studied in figure 21. The energy absorption and energy dissipation quantities have been computed using the trapezoidal numerical integration method implemented in MATLAB. The preliminary conclusion drawn from this figure is that more energy is dissipated than absorbed for all lattice structures and fiber volume fractions due to the presence of plastic hardening behavior of the composite. The energy dissipated by both re-entrant meta-composite with 20 and 40 wt% is calculated as 0.13 $\pm$ 0.02 J while their hexagonal counterparts result in 0.48 $\pm$ 0.02 J and 0.51 $\pm$ 0.05 J energy dissipation. On the other hand, the energy absorbed by the re-entrant meta-composite with 20 and 40 wt% is calculated as 0.03 $\pm$ 0.005 J

Table 7. Shape recovery behavior of meta-structures with different patterns and fiber volume fractions under the compression load.

Label	Length of samples before loading (mm)	Length of samples after unloading (mm)	Length of samples after heating- cooling (mm)	Shape recovery (%)
R0	30.3 ± 0.1	24.2 ± 0.5	30.3 ± 0.4	100
R1	31.8 ± 0.3	26.7 ± 1.0	30.1 ± 0.8	95
R2	32.7 ± 0.4	26.1 ± 1.1	30.8 ± 1.1	94
H0	29.9 ± 0.1	24.1 ± 0.4	29.8 ± 0.5	100
H1	29.7 ± 0.2	25.1 ± 0.9	28.4 ± 0.9	96
H2	31.3 ± 0.4	24.5 ± 0.7	29.7 ± 0.9	95

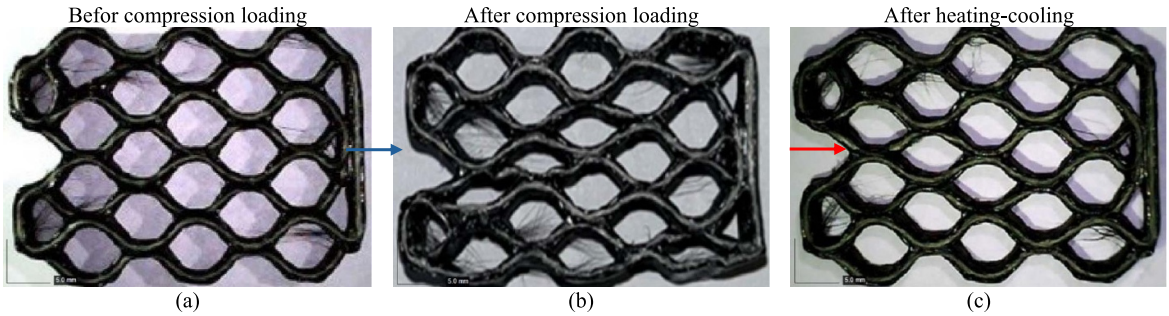

Figure 22. The configuration of the hexagonal meta-structure with 20 wt% of glass fiber: (a) before compression loading, (b) after compression loading-unloading, (c) after heating-cooling showing 96% shape recovery.

Table 8. Shape recovery behavior of meta-structures with different patterns and fiber volume fractions under bending.

Label	Bending angle after loading	Bending angle after heating- cooling	Shape recovery (%)
R0	19 ± 0.8	0.2 ± 0.2	99
R1	18 ± 1.1	1.4 ± 0.9	92
R2	16 ± 0.9	2.1 ± 1.1	87
H0	18.8 ± 0.9	0.5 ± 0.5	97
H1	17.5 ± 0.7	1.9 ± 1.1	89
H2	15.9 ± 1.2	2.3 ± 1.7	86

and 0.04 ± 0.007 J while both hexagonal counterparts result in 0.10 ± 0.007 J energy absorption.

3.6. Shape recovery

Table 7 represents the shape recovery feature of samples with different fiber volume fractions and patterns under a compression load. The preliminary conclusion drawn from table 7 is that by increasing the fiber volume fraction, the shape recovery decreases as expected. The main reason for the shape recovery is the shape memory feature of PLAs, therefore by decreasing the amount of matrix, the shape recovery of composite decreases as well. The non-reinforced hexagonal and re-entrant patterns possess the highest shape recovery (100%) and the reinforced re-entrant pattern with 40 wt% of glass fiber has the lowest shape recovery (94%). Figure 22 illustrates a sample with a hexagonal pattern and 20 wt% of glass fiber, before loading, at the end of the loading-unloading, and at the end of the heating-cooling step. It is seen that the meta-structure has capability to release the residual plastic deformation parietally and recover its original shape (96%).

Next, the shape recovery feature of the meta-structures under bending is investigated. Table 8 lists the shape recovery ratio of samples with different fiber volume fractions and patterns under bending. It can be found that increasing the volume fraction of glass fiber decreases the shape memory of composites as expected. The non-reinforced samples show the highest shape recovery ratio near to 100%. The re-entrant pattern with 20 wt% of glass fiber results in the highest shape recovery ratio (92%) among other reinforced samples. In contrast, the hexagonal pattern with 40 wt% of glass fiber has the lowest shape recovery ratio (86%). Figure 23 presents a sample with a hexagonal pattern and 20 wt% of glass fiber, before bending, after bending, and at the end of the heating-cooling step. It can be observed that the meta-structure releases the residual plastic deformation parietally and recovers its original shape (89%).

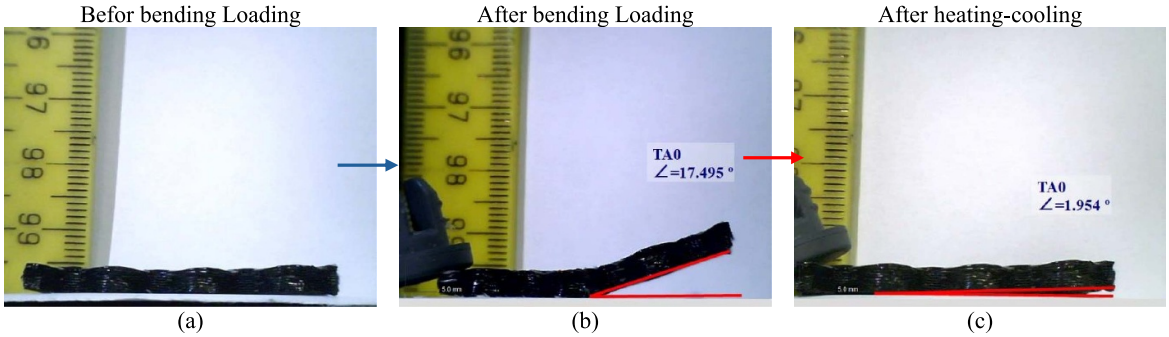

Figure 23. The configuration of the hexagonal meta-composite with 20 wt% of glass fiber: (a) before bending, (b) after bending, (c) after heating-cooling showing 74% shape recovery.

4. Conclusion

This research introduced a groundbreaking approach to 3D/4D printing recoverable, energy-absorbing meta-composites reinforced with continuous glass fiber via FDM technology. The newly developed G-code modifier software introduced in this study successfully and automatically detects geometrical edges, even in complex structures such as meta-materials, using a robust algorithm that precisely identifies curves and sharp turns. This algorithm enables localized reduction of printing speed, significantly improving fiber placement and printing accuracy in critical regions. This innovation enables the efficient manufacturing of high-performance meta-composites, overcoming key challenges in continuous fiber-reinforced AM. While this work focused mainly on validating the accuracy improvements achieved with the compocode, future studies are required to fully quantify its impact on the mechanical performance. In this study, the mechanical performance of hexagonal and re-entrant meta-composite structures, reinforced with varying glass fiber volume fractions (0, 20, and 40 wt%), was systematically investigated under tensile, compression, and bending loadings. Tensile, bending and compression strength of meta-composites increase by 1000%, 1000% and 450% compared to non-reinforced meta-structures, respectively. The hexagonal pattern with 40 wt% glass fiber demonstrated superior tensile (2800 N) and bending (200 N) strength, while the re-entrant structure with 40 wt% exhibited exceptional compressive strength (400 N) and a stable quasi-constant force plateau, indicative of efficient energy absorption and steady zero-stiffness behavior before densification. This quasi-zero stiffness regime highlights the capacity of the re-entrant pattern to deform steadily under constant force, making it ideal for energy absorption applications. Energy dissipation and absorption were maximized in the hexagonal meta-composite at 40 wt%, with values of 0.51 J and 0.10 J, respectively. Additionally, shape recovery tests demonstrated impressive recoverability, with non-reinforced and reinforced meta-composites achieving ∼100% and 95% recovery under compression. Although bending recovery was lower, the results underscore the synergy between meta-material design, continuous fiber reinforcement, and advanced software-driven manufacturing. This study closes a critical gap in the field, introducing a powerful framework for creating versatile and high-performance meta-composites. These findings advance the state of 3D/4D printing and open avenues for applications in energy absorption systems, aerospace, automotive and biomedical devices, significantly contributing to composite science and engineering.

Data availability statement

All data that support the findings of this study are included within the article.

Acknowledgments

The authors would like to gratefully acknowledge the support by the UK Engineering and Physical Sciences Research Council (EPSRC) (Award No.: EP/Y011457/1) and the RAEng/Leverhulme Trust Research Fellowship (Award No.: LTRF-2324–20–129, Researcher: Mahdi Bodaghi).

Author contributions

O Kordi 0000-0003-1618-1806
Conceptualization (supporting), Data curation (lead), Formal analysis (lead), Investigation (supporting), Methodology (supporting), Validation (equal), Visualization (lead), Writing – original draft (lead), Writing – review & editing (supporting)

M Yusefi Passandi 0009-0000-5418-7681
Data curation (supporting), Investigation (supporting), Visualization (supporting), Writing – review & editing (supporting)

A H Behravesh 0000-0003-3089-5709
Investigation (supporting), Methodology (supporting), Supervision (supporting), Writing – review & editing (supporting)

M Bodaghi 0000-0002-0707-944X
Conceptualization (lead), Data curation (supporting), Funding acquisition (lead), Investigation (lead), Methodology (lead), Project administration (lead), Supervision (lead), Validation (equal), Writing – original draft (supporting), Writing – review & editing (lead)

References

[1] Askari M *et al* 2020 Additive manufacturing of metamaterials: a review *Addit. Manuf.* **36** 101562
[2] Paul D D 2010 *Optical Metamaterials: Fundamentals and Applications* (American Institute of Physics)
[3] Saxena K K, Das R and Calius E P 2016 Three decades of auxetics research− materials with negative poisson's ratio: a review *Adv. Eng. Mater.* **18** 1847–70
[4] Mirabolghasemi A, Akbarzadeh A H, Rodrigue D and Therriault D 2019 Thermal conductivity of architected cellular metamaterials *Acta Mater.* **174** 61–80
[5] Li X, Gao L, Zhou W, Wang Y and Lu Y 2019 Novel 2D metamaterials with negative Poisson's ratio and negative thermal expansion *Extreme Mech. Lett.* **30** 100498
[6] Chen Y, Li T, Scarpa F and Wang L 2017 Lattice metamaterials with mechanically tunable poisson's ratio for vibration control *Phys. Rev. Appl.* **7** 024012
[7] Bodaghi M, Damanpack A R, Hu G F and Liao W H 2017 Large deformations of soft metamaterials fabricated by 3D printing *Mater. Des.* **131** 81–91
[8] Moscatelli M, Ardito R, Driemeier L and Comi C 2019 Band-gap structure in two-and three-dimensional cellular locally resonant materials *J. Sound Vib.* **454** 73–84
[9] Nimmagadda C and Matlack K H 2019 Thermally tunable band gaps in architected metamaterial structures *J. Sound Vib.* **439** 29–42
[10] Jiao P and Alavi A H 2021 Artificial intelligence-enabled smart mechanical metamaterials: advent and future trends *Int. Mater. Rev.* **66** 365–93
[11] Zheng X *et al* 2016 Multiscale metallic metamaterials *Nat. Mater.* **15** 1100–6
[12] Kadic M, Milton G W, van Hecke M and Wegener M 2019 3D metamaterials *Nat. Rev. Phys.* **1** 198–210
[13] Al-Saedi D S, Masood S H, Faizan-Ur-Rab M, Alomarah A and Ponnusamy P 2018 Mechanical properties and energy absorption capability of functionally graded F2BCC lattice fabricated by SLM *Mater. Des.* **144** 32–44
[14] Zhao W, Liu L, Zhang F, Leng J and Liu Y 2019 Shape memory polymers and their composites in biomedical applications *Mater. Sci. Eng. C* **97** 864–83
[15] Kordi O, Behravesh A H, Hasannia S, Hedayati S K, Pourghaumi M, Mazdi M, Ghaderi I and Rizvi G 2023 Additive manufacture of PLLA scaffolds reinforced with graphene oxide nano-particles via digital light processing (DLP) *J. Biomater. Appl.* **38** 484–99
[16] Svensson E 2017 Material characterization of 3D-printed energy-absorbent polymers inspired by nature
[17] Liu R, Ji C, Zhao Z and Zhou T 2015 Metamaterials: reshape and rethink *Engineering* **1** 179–84
[18] Kumar R *et al* 2022 Overview on metamaterial: history, types and applications *Mater. Today Proc.* **56** 3016–24
[19] Gan Z, Zhuge Y, Thambiratnam D P, Chan T H, Zahra T and Asad M 2022 Recent advances in auxetics: applications in cementitious composites *Int. J. Prot. Struct.* **13** 295–316
[20] Haid D *et al* 2023 Mechanical metamaterials for sports helmets: structural mechanics, design optimisation, and performance *Smart Mater. Struct.* **32** 113001
[21] Góra P and Łopato P 2023 Metamaterials' application in sustainable technologies and an introduction to their influence on energy harvesting devices *Appl. Sci.* **13** 7742
[22] Bodaghi M, Serjouei A, Zolfagharian A, Fotouhi M, Rahman H and Durand D 2020 Reversible energy absorbing meta-sandwiches by FDM 4D printing *Int. J. Mech. Sci.* **173** 105451
[23] Sun S, An N, Wang G, Li M and Zhou J 2019 Snap-back induced hysteresis in an elastic mechanical metamaterial under tension *Appl. Phys. Lett.* **115** 091901
[24] Tan X, Chen S, Zhu S, Wang B, Xu P, Yao K and Sun Y 2019 Reusable metamaterial via inelastic instability for energy absorption *Int. J. Mech. Sci.* **155** 509–17
[25] Pa P *et al* 2012 Integrating metamaterials within a structural composite using additive manufacturing methods *Proc. 2012 IEEE Int. Symp. on Antennas and Propagation* (IEEE)
[26] Peltola S M, Melchels F P W, Grijpma D W and Kellomäki M 2008 A review of rapid prototyping techniques for tissue engineering purposes *Ann. Med.* **40** 268–80
[27] Hedayati S K, Behravesh A H, Hasannia S, Kordi O, Pourghaumi M, Saed A B and Gashtasbi F 2022 Additive manufacture of PCL/nHA scaffolds reinforced with biodegradable continuous fibers: mechanical properties, *in-vitro* degradation profile, and cell study *Eur. Polym. J.* **162** 110876
[28] Dawoud M, Taha I and Ebeid S J 2016 Mechanical behaviour of ABS: an experimental study using FDM and injection moulding techniques *J. Manuf. Process.* **21** 39–45
[29] Byberg K I, Gebisa A W and Lemu H G 2018 Mechanical properties of ULTEM 9085 material processed by fused deposition modeling *Polym. Test.* **72** 335–47
[30] Caminero M, Chacón J M, García-Moreno I and Reverte J M 2018 Interlaminar bonding performance of 3D printed continuous fibre reinforced thermoplastic composites using fused deposition modelling *Polym. Test.* **68** 415–23
[31] Lebedev S, Gefle O S, Amitov E T, Zhuravlev D V, Berchuk D Y and Mikutskiy E A 2018 Mechanical properties of PLA-based composites for fused deposition modeling technology *Int. J. Adv. Manuf. Technol.* **97** 511–8
[32] Ning F, Cong W, Qiu J, Wei J and Wang S 2015 Additive manufacturing of carbon fiber reinforced thermoplastic composites using fused deposition modeling *Composites B* **80** 369–78
[33] Bodaghi M, Rahmani K, Dezaki M L, Branfoot C and Baxendale J 2025 3D/4D printed bio-composites reinforced by bamboo charcoal and continuous flax fibres for superior mechanical strength, flame retardancy and recoverability *Polym. Test.* **143** 108709
[34] Akhoundi B, Behravesh A H and Bagheri Saed A 2019 Improving mechanical properties of continuous fiber-reinforced thermoplastic composites produced by FDM 3D printer *J. Reinf. Plast. Compos.* **38** 99–116
[35] Akhoundi B, Behravesh A H and Bagheri Saed A 2020 An innovative design approach in three-dimensional printing of continuous fiber–reinforced thermoplastic composites via fused deposition modeling process: in-melt simultaneous impregnation *Proc. Inst. Mech. Eng. B* **234** 243–59
[36] Akhoundi B, Nabipour M, Kordi O and Hajami F 2023 Calculating printing speed in order to correctly print PLA/continuous glass fiber composites via fused filament fabrication 3D printer *J. Thermoplast. Compos. Mater.* **36** 162–81
[37] Ghorbani F, Gharehbaghi H, Farrokhabadi A, Bolouri A, Behravesh A H and Hedayati S K 2024 Investigation of energy absorption performances of a 3D printed fiber-reinforced bio-inspired cellular structure under in-plane compression loading *Mech. Adv. Mat. Struct.* **31** 5234–52

[38] Quan Z, Liu C, Li J, Qin X and Yu J 2024 Fiber bundle deposition model and variable speed printing strategy for *in-situ* impregnation 3D printing of continuous fiber reinforced thermoplastic composites *Compos. Sci. Technol.* **255** 110723
[39] Xin X, Liu L, Liu Y and Leng J 2019 Mechanical models, structures, and applications of shape-memory polymers and their composites *Acta Mech. Solida Sin.* **32** 535–65
[40] Ding H, Zhang X, Liu Y and Ramakrishna S 2019 Review of mechanisms and deformation behaviors in 4D printing *Int. J. Adv. Manuf. Technol.* **105** 4633–49
[41] Bodaghi M and Liao W 2019 4D printed tunable mechanical metamaterials with shape memory operations *Smart Mater. Struct.* **28** 045019
[42] Yang C, Boorugu M, Dopp A, Ren J, Martin R, Han D, Choi W and Lee H 2019 4D printing reconfigurable, deployable and mechanically tunable metamaterials *Mater. Horiz.* **6** 1244–50
[43] Kaw A K 2005 *Mechanics of Composite Materials* (CRC Press)
[44] Bellehumeur C, Li L, Sun Q and Gu P 2004 Modeling of bond formation between polymer filaments in the fused deposition modeling process *J. Manuf. Process.* **6** 170–8
[45] Farah S, Anderson D G and Langer R 2016 Physical and mechanical properties of PLA, and their functions in widespread applications—A comprehensive review *Adv. Drug Deliv. Rev.* **107** 367–92
[46] Akhoundi B and Behravesh A H 2019 Effect of filling pattern on the tensile and flexural mechanical properties of FDM 3D printed products *Exp. Mech.* **59** 883–97
[47] Khan S, Joshi K and Deshmukh S 2022 A comprehensive review on effect of printing parameters on mechanical properties of FDM printed parts *Mater. Today Proc.* **50** 2119–27